Strål
säkerhets
myndigheten
Swedish Radiation Safety Authority

Author: Joel E. Geier

Technical Note

2012:67

Hydrogeological modelling of the Forsmark site

Report number: 2012:67 **ISSN:** 2000-0456
Available at www.stralsakerhetsmyndigheten.se

SSM perspektiv

Bakgrund

Strålsäkerhetsmyndigheten (SSM) granskar Svensk Kärnbränslehantering AB:s (SKB) ansökningar enligt lagen (1984:3) om kärnteknisk verksamhet om uppförande, innehav och drift av ett slutförvar för använt kärnbränsle och av en inkapslingsanläggning. Som en del i granskningen ger SSM konsulter uppdrag för att inhämta information i avgränsade frågor. I SSM:s Technical note-serie rapporteras resultaten från dessa konsultuppdrag.

Projektets syfte

Syftet med detta projekt är att genomföra en hydrogeologisk modellering av förvarsplatsen i Forsmark och att jämföra resultaten med SKB:s motsvarande resultat. Modelleringen utgår från SKB:s konceptuella modeller och parameteruppsättningar. Tillämpningen av de konceptuella modellerna sker dock med beräkningskoder som har utvecklats på uppdrag av SSM och skiljer sig således från SKB:s.

Slutrapporten från konsultprojektet (denna Technical Note) är ett av flera externa underlag som SSM kommer att beakta i sin egen granskning av SKB:s säkerhetsredovisningar, tillsammans med andra konsultrapporter, remissvar från en nationell remiss och en internationell expertgranskning av OECD:s kärnenergibyrå (NEA).

Författarens sammanfattning

En modelleringsstudie har genomförts med diskreta spricknätsverksmodeller (DFN) i kombination med modelleringsmetoder för att representera andra delar av berget som kan vara vattenförande, exempelvis den störda zonen kring deponeringstunnlar.

De huvudsakliga resultaten består av uppskattningar av bergets hydrauliska egenskaper och transportparametrar för DFN modeller på blockskalor av 50 m och 100 m. Resultaten innefattar också block som innehåller representativa segment av deponeringstunnlar med deponeringshål. Dessa blockskalor är representativa för diskretiseringen som används i SKB:s ECPM modeller (som representerar DFN egenskaperna med ett kontinuerligt poröst medium) för den tilltänkta förvarsplatsen i Forsmark som tillståndsansökan gäller.

Det genomförs simuleringar med analytiska, geometriska och permeameter-metoder för att på flera sätt uppskatta bergets effektiva hydrauliska egenskaper och transportparametrar samt för att förstå resultatens signifikans.

De geometriska uppskattningarna av den hydrauliska konduktiviteten, porositeten och flödesvätta ytan på 50 m och 100 m blockskalorna är jämförbara med analytiska uppskattningarna som grundas på modeller för sprickor med oändlig utsträckning. Däremot är de geometriska uppskattningarna som tar hänsyn till sprickornas ändliga utsträckning och den stokastiska variationen mellan block typiskt sett lägre and de analytiska uppskattningarna av egenskaperna för samma djupintervall.

Jämförelsen av de geometriska uppskattningarna med permeameteruppskattningarna för DFN modellerna och de givna blockskalorna visar att de geometriska uppskattningarna av hydrauliska konduktiviteten (medelvärdesbildad över de tre koordinatriktningarna) tenderar att vara högre än permeameteruppskattningarna. Skillnaden är ungefär en storleksordning för den lägre endan av hydrauliska konduktivitetsspannet medan en bättre överensstämmelse fås för de mer konduktiva blocken.

Dessa resultat pekar på möjligheten att använda geometriska uppskattningar – möjligtvis med en empirisk anpassning för block med låga K värden – som en relativt effektiv metod för att simulera hydrauliska konduktivitetsfält för grundvattenflödesmodeller som baseras på kontinuummetoder.

Den geometriska metodens begränsningar identifieras ifråga om spännvidd och typ av anisotropi som kan skapas. Permeametersimuleringarna pekar på att det sannolikt finns block med en effektiv hydraulisk konduktivitet som är mer ensriktad än vad som kan fås med den geometriska uppskattningsmetoden. Därför krävs den mer beräkningsintensiva permeametermetoden om anisotropins roll på blockskala ska utvärderas för förvarsplatsskalemodellerna.

Fluxviktade uppskattningar av porositet och flödesvätt yta från permeametersimuleringar befinns tre till fyra storleksordningar lägre än motsvarande geometriska uppskattningar beroende på viktningsmetod. De fluxviktade uppskattningarna är sannolikt mer representativa för delarna av spricknätverket som skulle bli genomflödade av radionuklider från slutförvaret även om man inte beaktar fysikalisk kanalbildning. Lägre värden av dessa parametrar kan leda till uppskattningar av mindre retention i geosfären. Det framstår därmed som viktigt att granska hur de effektiva värdena för dessa egenskaper har härletts i tillämpningen av ECPM modellerna för förvarsplatsen i Forsmark.

Simuleringar av flödet runt en deponeringstunnel i blockskalesimuleringarna av det diskreta spricknätverket på förvarsdjup pekar på att även en skadezon som delvis inte är sammanhängande kan ha en signifikant påverkan på den hydrauliska konduktiviteten i riktningen parallellt till tunnelaxeln. Detta beror till synes på en utökad konnektivitet av spricknätverket. Däremot är skadezonens påverkan på flödet i andra riktningar försumbar.

Transportsimuleringar på blockskala med hjälp av partikelspårning pekar på att en skadezon i en deponeringstunnels sula, given dess existens, är den huvudsakliga flödesvägen för advektiv-dispersiv transport. Blockskalesimuleringarna stöder tidigare resultat från modellering på förvarsområdesskala som pekar på att partiklar som släpps från ett deponeringshål tenderar att flöda till nästa deponeringshål i det glesa spricknätverket som har tolkats föreligga på förvarsdjup i Forsmark. En mindre sammanhängande skadezon kan leda till komplexare flödesvägar mellan deponeringshålen. I fall där sammanhållningen av skadezonen sett per yta är 50 % eller större är däremot påverkan på resultaten för transportmotståndet på blockskala inte särskilt stora.

Uppskattningarna av hydrauliska konduktiviteten, porositeten och flödesvätta ytan på blockskala från denna studie stämmer i stora drag överens med motsvarande resultat från SKB:s hydrogeologiska modeller för SR-Site. SKB har inte redovisat information för anisotropi på blockskala på ett sätt som direkt kan jämföras med resultaten från denna studie. Studiens resultat pekar dock på att den geometriska uppskattningsmetoden (som används i hydro-DFN kalibreringsprocessen) tenderar att underskatta förhållandet mellan horisontal och vertikal hydraulisk konduktivitet jämfört med permeameteruppskattningar. SKB har inte redovisat porositet och flödesvätt yta som motsvarar de fluxviktade uppskattningarna som presenteras i denna studie. Dessa fluxviktade uppskattningarna tar hänsyn till sannolikheten att största delen av vattnet som rör sig genom berget endast kommer i kontakt med en liten del av spricknätverket. En jämförelse av resultat är därför ej möjlig.

Blockskalesimuleringarna av inflödet till simulerade tunnlar och deponeringshål ger resultat som i stora drag överensstämmer med SKB:s resultat som har beräknats med mer komplexa och rumsligt mer omfattande modeller. Transportmotståndet (F) i blockskalesimuleringarna för skalor som närmar sig 100 m överensstämmer också i stora drag med F värdena för motsvarande delar av SKB:s DFN modeller.

Den generella överensstämmelsen av resultaten från denna studie med SKB:s resultat följer ur beräkningar som grundar sig i SKB:s konceptuella modeller. Modelleringarna skiljer sig endast i den numeriska tillämpningen av de konceptuella modellerna. Alternativa konceptuella DFN modeller, exempelvis sådana som har tillämpats i en tidigare studie av Geier (2011), skulle kunna leda till större skillnader.

Projektinformation
Kontaktperson på SSM: Georg Lindgren
Diarienummer ramavtal: SSM2011-3628
Diarienummer avrop: SSM2011-4284
Aktivitetsnummer: 3030007-4016

SSM perspective

Background

The Swedish Radiation Safety Authority (SSM) reviews the Swedish Nuclear Fuel Company's (SKB) applications under the Act on Nuclear Activities (SFS 1984:3) for the construction and operation of a repository for spent nuclear fuel and for an encapsulation facility. As part of the review, SSM commissions consultants to carry out work in order to obtain information on specific issues. The results from the consultants' tasks are reported in SSM's Technical Note series.

Objectives of the project

The objective of this project is to perform a hydrogeological modelling of the Forsmark repository site to compare the results with SKB's respective results. The modelling is based on SKB's conceptual models and parameter sets. The implementation of the conceptual models is, however, carried out with a computer code that has been developed for SSM and thus differs from SKB's.

The final report from this consultant project (this Technical Note) is one of several documents with external review comments that SSM will consider in its own review of SKB's safety reports, together with other consultant reports, review comments from a national consultation, and an international peer review organized by OECD's Nuclear Energy Agency (NEA).

Summary by the author

A modelling study has been conducted using discrete-fracture network (DFN) models in combination with discrete-feature hydrogeological modelling methods for representation of other potentially conductive features such as the disturbed zone around repository tunnels.

The principal results consist of hydraulic and transport property estimates for discrete-fracture network (DFN) models on block scales of 50 m and 100 m, including blocks containing representative segments of deposition tunnels with deposition holes. These block scales are representative of the discretization used in equivalent continuum porous medium (ECPM) models of the Forsmark site in support of the license application.

Analytical, geometrical, and permeameter simulation methods are used to give multiple methods for estimating effective properties and understanding the significance of results.

Geometrical estimates of hydraulic conductivity, porosity and wetted surface for 50 m and 100 m block scales are comparable to analytical estimates based on models for fractures of infinite extent. However, the geometrical estimates of these properties, which take into account the finite extent of fractures as well as stochastic variation between blocks, are typically lower than the analytical estimates for the same depth intervals.

Comparison of geometrical estimates with permeameter simulations show that, for the DFN models and block scales, the geometrical estimates of hydraulic conductivity (averaged over the three coordinate directions) tend to be higher than the permeameter estimates by about an order of magnitude for the lower part of the hydraulic conductivity range, but show better agreement for the more conductive blocks.

These results indicate a possibility to use geometrical estimation – possibly with an empirical adjustment for the lower-K blocks – as a relatively efficient method for simulating hydraulic conductivity fields for groundwater flow models based on continuum concepts.

However, limitations of the method are also identified in terms of the range and types of anisotropy that can be produced. Permeameter simulations indicate a likelihood of blocks for which the effective hydraulic conductivity is more strongly unidirectional than can be produced by the geometrical estimation method. Therefore, if the role of block-scale anisotropy for site-scale models is to be assessed as part of license application review, more computationally intensive approaches such as permeameter simulations will be required.

Flux-weighted estimates of porosity and wetted surface from permeameter simulations are found to be lower than the corresponding geometrical estimates of these parameters, by 3 to 4 orders of magnitude depending on the method of weighting. The flux-weighted estimates are likely to be more representative of the fraction of the fracture network that would be encountered by radionuclides released from the repository, even without taking physical channelling into account. Lower values of these parameters can lead to reduced estimates of geosphere retention. Hence it appears to be important to review how effective values of these properties are derived for use in ECPM models of the Forsmark site.

Simulations of flow for a deposition tunnel embedded in block-scale simulations of the DFN at repository depth indicate that even an EDZ that is partly discontinuous can have a significant effect on directional hydraulic conductivity parallel to the tunnel axis, apparently by increasing connectivity of the fracture network. However, the influence of the EDZ for flow in other directions is negligible.

Block-scale transport simulations by particle tracking indicate that an EDZ in the floor of a deposition tunnel, when present, is the dominant path for advective-dispersive transport. The block-scale simulations support previous site-scale modelling results which indicated that particles released from one deposition hole tend to migrate to the next deposition hole, for the sparsely fractured rock mass that is interpreted to exist at repository depths at Forsmark. Reduction of continuity of the EDZ can lead to more complex solute trajectories in this direction. However for cases in which the areal persistence of the EDZ is 50% or greater, the results in terms of transport resistance on the block scale are not strongly affected.

The block-scale estimates of hydraulic conductivity, porosity, and flow wetted surface from this study are broadly consistent with the comparable results from SKB's hydrogeological models for SR-Site. SKB has not presented comparable information about block-scale anisotropy, but the results obtained here indicate that the geometrical estimation method (as used in the hydro-DFN calibration process) tends to underestimate the ratio of horizontal to vertical hydraulic conductivity, in comparison with permeameter estimates. SKB also has not produced porosity and flow wetted surface estimates equivalent to the flux-weighted estimates presented here, which account for the likelihood that most water moving through the rock comes into contact with only a small portion of the fracture network.

Block-scale simulations to simulated tunnels and deposition holes in the present study yield distributions of inflows that are reasonably similar to those predicted by SKB's more complex, larger-scale models. Transport resistances (F) for scales approaching 100 m, in the block-scale simulations, are also broadly similar to F values for the DFN portion of SKB's models.

The broad consistency with SKB's results obtained in this study follows from a model that is based on SKB's underlying DFN conceptual model, although different in terms of the details of numerical implementation. Alternative DFN conceptual models such as considered in a previous study (Geier, 2011) could yield larger differences.

Project information

Contact person at SSM: Georg Lindgren

Strål
säkerhets
myndigheten
Swedish Radiation Safety Authority

Author: Joel E. Geier
Clearwater Hardrock Consulting, Corvallis, Oregon, U.S.A.

Technical Note 39

2012:67

Hydrogeological modelling of the Forsmark site

Date: November 2012
Report number: 2012:67 **ISSN:** 2000-0456
Available at www.stralsakerhetsmyndigheten.se

Content

1. Introduction

This modeling project was undertaken to support review of the license application and safety case for a proposed high-level radioactive-waste repository at the Forsmark site in northern Uppland, Sweden. The general goal is to to achieve broad understanding of hydrogeological aspects of SR-Site within a limited time frame, making use of relatively simple, block-scale DFN models.

The following issues for investigation were identified based on a preliminary reading of relevant sections of the SR-Site main report and data report (SKB TR-11-01 & SKB TR-10-52):

- Reasonableness of equivalent continuum properties (hydraulic conductivity tensors, porosities, and flow wetted surface) to represent the rock mass in large-scale hydrogeological simulations;
- Interaction of natural fractures in the rock mass in combination with the excavation-disturbed zone (EDZ) along deposition tunnels, as pathways for groundwater flow and radionuclide transport;
- Sensitivity of rock-mass hydraulic properties to predicted stress conditions during future glaciations;
- Reasonableness of predicted ranges of groundwater flux to deposition holes;
- Reasonableness of predicted ranges of transport resistance and locations for discharge for radionuclide transport pathways from the repository.

These issues are addressed here primarily by a combination of analytical methods, block-scale DFN geometrical calculations, and block-scale flow and transport simulations using a discrete-feature model.

2. Methodology

2.1. Discrete-fracture network models

The calculations for the present study use a statistical, discrete-fracture network (DFN) characterization of fractures and minor deformation zones smaller than 1 km scale. The DFN submodel of these features is a stochastic component of the discrete-feature model. Stochastic realizations of the DFN component are generated by simulation, using a different seed value for the random number generator to produce each realization. The DFN submodel is defined in terms of statistical distributions of fracture properties (location, size, orientation, transmissivity etc.) for 4 to 5 sets of fractures within each rock domain. The statistical distributions used in the present study are described in Section 3.4.2.

The primary tool used for block-scale and site-scale model calculations is the discrete-feature modelling software package, DFM (Geier, 2008). Analytical methods as detailed below are used for bounding calculations and for scoping of sensitivities.

DFM model setups as used for previous modeling of SDM-Site Forsmark (Geier , 1010; Geier, 2011) have been used a a starting point, after adjusting for consistency with the data that are cited for SR-Site (SKB R-09-22, SKB TR-10-52, and background reports).

2.1.1. Fracture domains

The fracture domains as defined for SDM-Site Forsmark (SKB, 2008) were obtained as part of a data delivery from SKB's SICADA database and transformed to AutoCAD DXF format by Geosigma AB. The special-purpose script *parsedomains* was used to convert these to DFM panel format, resulting in the data file:

FD_FM_reg_v22_basemod.pan .

Next these were translated into polyhedral domains for generating fractures with the *DFM* module *fracgen*, resulting in the file:

FM_reg_v22_basemod.domains

which contains all of the fracture domains defined by SKB. Input files for each specific domains were produced by hand-editing copies of this file to delete all other domains. Finally, subdomains for different depths as specified in Table C-1 of SKB R-08-95 (Follin, 2008) were defined by running the script *create_depth_domains* which inserts the appropriate *fracgen* clipping commands, as detailed in Table 2.1.

Fracture Domains	Depth Subdomain	*fracgen* clipping commands
FFM01 and FFM06	shallow	clipped below -200
	middle	clipped above -200 clipped below -400
	deep	clipped above -400
FFM02	shallow	(*none needed as FFM02 only exists above –200 m*)
FFM03, FFM04 and FFM05	shallow	clipped below -400
	deep	clipped above -400

Table 2.1 Definition of fracture subdomains by depth. Note that the depth ranges for subdomains in FFM06 are the same as for FFM01, and the depth ranges for subdomains in FFM04 and FFM05 are the same as for FFM03.

2.1.2. Fracture set definitions

The fracture population for the Forsmark model is simulated based on the statistical hydro-DFN model as specified in SKB R 08-98 Table C-1 (Follin, 2008). The fracture set statistics listed in that table were transcribed directly into fracture set definitions files for fracgen input, as listed in Table 2.2.

Fracture Domains	Depth Subdomain	Fracture set definitions file
FFM01 and FFM06	shallow	FFM01shallow.sets
	middle	FFM01middle.sets
	deep	FFM01deep.sets
FFM02	shallow	FFM02shallow.sets
FFM03, FFM04 and FFM05	shallow	FFM03shallow.sets
	deep	FFM03deep.sets

Table 2.2 List of fracture set definitions files used as input to *fracgen*, for generating fractures in the different fracture domains and subdomains.

2.2. Estimation of effective continuum properties

Three methods are applied to evaluate rock-mass hydraulic conductivity tensors *K*, porosities θ, and flow wetted surface a_r for the DFN models used in SR-Site:

- Analytical and semi-analytical formulae for the contribution of each fracture set to the aggregate hydraulic properties, based on an assumption of fractures of infinite extent in an infinite domain;
- Block-scale DFN geometrical calculations based on summing the contributions of individual fractures for 20 m to 100 m block scales;
- Block-scale DFN flow (permeameter) simulations.

The first two methods do not account for fracture connectivity effects, but provide quick approximations that can be used for scoping sensitivities. The semi-analytical methods apply to infinite domains rather than finite blocks, and thus do not account for scale effects or heterogeneity. The last method is more computationally intensive but is necessary to assess the validity of a **K** tensor in a sparsely connected DFN. Formulae and procedures for each of these methods are discussed in the following paragraphs.

2.2.1. Analytical estimates of rock hydraulic properties

A simple analytical estimate of the flow wetted surface, a_r is obtained directly from the conductive fracture intensity as:

$$a_r = 2\mathrm{P}_{32\mathrm{c}}$$

summed over the fracture sets for a given fracture domain.

An analytical or semi-analytical estimate of the flow porosity θ can be obtained by integrating over the fracture transport aperture distribution to find the arithmetic mean aperture, and multiplying this by the areal intensity of conductive fractures per unit rock volume:

$$\theta_r = P_{32\mathrm{c}}\bar{b}_T$$

For simple cases where aperture is independent of other fracture properties, the mean aperture can be found analytically as the first moment of the probability density function for aperture:

$$\bar{b}_T = P_{32\mathrm{c}}\int_0^\infty b_T f_b(b_T)\,db_T$$

In SKB's SR-Site models, the transport aperture b_T is considered to be related to fracture transmissivity *T* by an empirical relationship $b_T = b_T(T)$, specifically:

$$b_T[\mathrm{mm}] = 0.5\left(T\left[m^2/s\right]\right)^{0.5}$$

Fracture transmissivities are simulated based on a variety of correlation relationships with the fracture size (radius) *r* as the primary variable. For the cases in which there is a direct functional relationship between *T* and *r*, this gives the possibility of a fully analytical solution based on:

$$\bar{b}_T = P_{32\mathrm{c}} \int_0^\infty b_T\left(T(r)\right) f_r(r)\, dr$$

More generally (for example the case where T and r are semicorrelated), the mean aperture can be estimated numerically by stochastic sampling of the fracture size distribution:

$$\langle \bar{b}_T \rangle_N = \frac{1}{N} \sum_{i=0}^{N} b_T\left(T\left(r_i\right)\right)$$

where r_i is the ith random sample from the size distribution $f_r(r)$. However, this type of estimate exaggerates the effect of the small-radius, small-aperture fractures and thus leads to an underestimate of porosity. A more appropriate average aperture is weighted with respect to fracture area

$$\langle \bar{b}_T \rangle_A = \frac{\sum_{i=0}^{N} A\left(r_i\right) b_T\left(T\left(r_i\right)\right)}{\sum_{i=0}^{N} A\left(r_i\right)}$$

where for circular fractures $A(r_i) = \pi$.. This area-weighted estimate is used in the present study.

An analytical estimate of the hydraulic tensor **K** due to a set of fractures with orientations the Fisher distribution fractures is obtained starting from the expression of Snow (1969) for the hydraulic conductivity tensor due to a set of parallel, infinite, uniformly spaced fractures, which may be written in matrix notation as:

$$K = \frac{T}{s}\left[I - n \otimes n\right]$$

where:

T = fracture transmissivity

s = effective fracture spacing

I = the identity matrix with components $I_{ii} = 1$; $I_{ij} = 0$ for $i \neq j$; $i,j = 1,2,3$,.

$\boldsymbol{n}$ = unit normal vector to fracture plane (*i.e.*, the fracture pole)

and where $n \otimes n$ denotes the outer (tensor) product with components $n_i\, n_j$, for i, j = 1, 2, 3.

For a set of fractures of infinite extent with poles (normal vectors) distributed according to a Fisher distribution:

$$f\left(\theta, \phi; \kappa\right) = c\left(\kappa\right) e^{\kappa \cos\theta}$$

where:

θ = angle from the mean pole direction of the fracture set.

ϕ = angle in the longitudinal sense about the mean pole,

and:

$$\frac{1}{c\left(\kappa\right)} = \int_0^{2\pi} \int_0^{\pi} e^{\kappa \cos\theta} \sin\theta\, d\theta\, d\phi = \frac{4\pi \sinh\left(\kappa\right)}{\kappa}$$

and assuming that fracture transmissivity is independent of orientation, the effective hydraulic conductivity tensor is found by integrating the differential contribution of each fracture orientation over the unit sphere:

$$K = \frac{\bar{T}}{P_{32\mathrm{c}}} c\left(\kappa\right) \int_0^{2\pi} \int_0^{\pi} \left[I - n \otimes n\right] e^{\kappa \cos\theta} \sin\theta\, d\theta\, d\phi$$

where $\bar{T}$ is the arithmetic mean transmissivity of the fracture set, and P_{32c} is used in place of *s* as a directionally unbiased measure of spacing.

If we choose a working right-handed coordinate system (x_1', x_2', x_3') such that x_3' is parallel to the mean pole of the Fisher distribution θ = 0 and x_1' coincides with $\phi = 0$, then the matrix inside the integral may be written term-by-term as:

$$[I - n \otimes n] = \begin{bmatrix} 1-\sin^2\theta\cos^2\phi & \sin^2\theta\sin\phi\cos\phi & \sin\theta\cos\theta\cos\phi \\ \sin^2\theta\sin\phi\cos\phi & 1-\sin^2\theta\sin^2\phi & \sin\theta\cos\theta\sin\phi \\ \sin\theta\cos\theta\cos\phi & \sin^2\theta\sin\phi\cos\phi & 1-\cos^2\theta \end{bmatrix}$$

Substituting this into the matrix integrand of the preceding equation and integrating term-by-term yields the hydraulic conductivity tensor $\mathbf{K}'$ in the Fisher-aligned coordinate system (x_1', x_2', x_3'):

$$K' = \frac{\bar{T}}{P_{32c}} \begin{bmatrix} 1-\pi c(\kappa)B(\kappa) & 0 & 0 \\ 0 & 1-\pi c(\kappa)B(\kappa) & 0 \\ 0 & 0 & 2\pi c(\kappa)B(\kappa) \end{bmatrix}$$

where:

$$B(\kappa) = \int_0^{\pi} \sin^3\theta e^{\kappa cos\theta}\, d\theta = \frac{4}{\kappa^2}\left[\cosh\kappa - \frac{\sinh\kappa}{\kappa}\right]$$

$$c(\kappa) = \frac{\kappa}{4\pi\sinh(\kappa)}$$

This can be simplified and written more compactly as:

$$K' = \begin{bmatrix} K_t & 0 & 0 \\ 0 & K_t & 0 \\ 0 & 0 & K_p \end{bmatrix}$$

where:

$$K_t = \frac{\bar{T}}{P_{32c}}\left[1 - \frac{\coth\kappa}{\kappa} + \frac{1}{\kappa^2}\right]$$

$$K_p = \frac{2\bar{T}}{P_{32c}}\left[\frac{\coth\kappa}{\kappa} - \frac{1}{\kappa^2}\right]$$

are the components of hydraulic conductivity transverse and parallel, respectively, to the mean pole of the Fisher distribution.

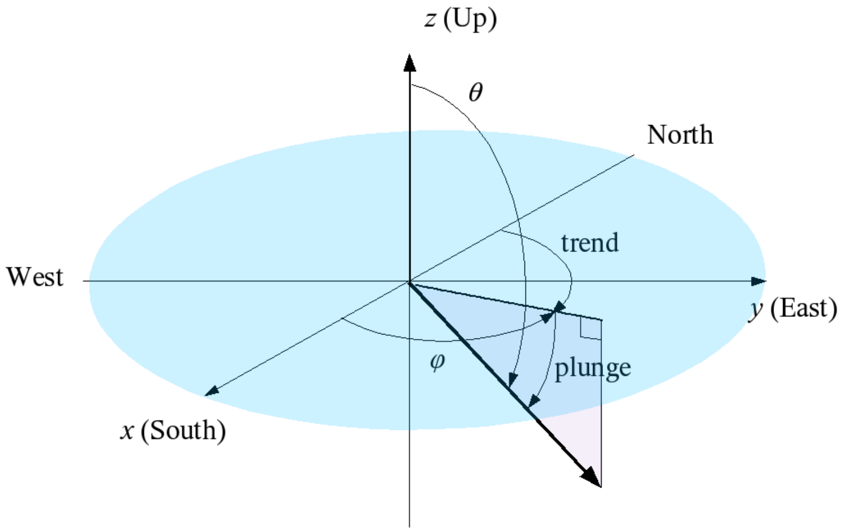

Figure 2.1. Spherical polar coordinate system.

For the general situation, the components of the hydraulic conductivity tensor may be required for a reference coordinate system (x_1, x_2, x_3) or (x, y, z) which is not necessarily aligned with the mean pole of the Fisher distribution. Assuming that the mean pole is specified in spherical polar coordinates (Figure 2.1)as (θ_m,ϕ_m) where θ_m is the angle from the x_3 direction (typically vertical) to the mean pole direction, and ϕ_m)is the angle from the x_1 direction to the projection of the mean pole into the x_1 – x_2 plane, then by defining the rotation matrix **A** as:

$$A = \begin{bmatrix} \cos\theta_m \cos\phi_m & -\sin\phi_m & \sin\theta_m \cos\phi_m \\ \cos\theta_m \sin\phi_m & \cos\phi_m & \sin\theta_m \sin\phi_m \\ -\sin\theta_m & 0 & \cos\theta_m \end{bmatrix}$$

the hydraulic conductivity tensor in the reference coordinate system may be obtained as :

$$K = \mathbf{AK}'A^T$$

where the superscript T denotes the matrix transpose.

To obtain an analytical estimate of the hydraulic conductivity tensor for a fracture domain that contains multiple fracture sets, each with its own Fisher distribution parameters (mean pole direction and concentration), mean transmissivity, and P_{32c}, the overall **K** tensor is calculated as the sum of the **K** tensors to each set.

Analogous to the calculation of a mean aperture, an area-weighted estimate of the mean transmissivity for use in the above analytical formulae can be obtained from simulations as:

$$\langle \bar{T} \rangle_A = \frac{\sum_{i=0}^{N} A(r_i) T(r_i)}{\sum_{i=0}^{N} A(r_i)}$$

2.2.2. Geometrical estimates of rock hydraulic properties

Block-scale estimates of the rock mass hydraulic properties **K**, θ, and a_r can also be produced using geometrical calculations based stochastic simulations of the DFN model. In contrast to the foregoing analytical/semi-analytical methods, this approach accounts for the effects of finite fracture size and finite block scales, and produces estimates of spatial variability. However, as for the analytical methods, the geometrical methods described here do not account for connectivity effects.

The basic approach in producing geometrical estimates of rock-mass hydraulic properties is to add up the contributions of individual fractures for 20 m to 100 m block scales. For these calculations, realizations of the complete site-scale DFN model are used, and properties are calculated for blocks at different positions in the reference coordinate system.

The contribution of a single fracture *i* to the block-scale tensor **K** is calculated from Snow's law (Snow, 1969) which, as in the preceding section, can be written in matrix form as:

$$K_i = \frac{T_i}{s_i}\left[I - n \otimes n\right]$$

where:

T_i = fracture transmissivity
s_i = effective fracture spacing
$\mathbf{I}$ = the identity matrix with components $I_{ii} = 1$; $I_{ij} = 0$ for $i \neq j$; $i,j = 1,2,3,$.
$\boldsymbol{n}$ = unit normal vector to fracture plane

and where $n \otimes n$ denotes the outer (tensor) product with components $n_i n_j$, for $i, j = 1, 2, 3$.

The effective fracture spacing s_i is taken as V/A_i where A_i is the area of the fracture that lies within the volume V of the rock block (the entire area of the fracture, if the fracture is entirely within the rock block).

The block-scale hydraulic conductivity tensor is then approximated as the sum of the contributions of each fracture that has some portion within the block volume V:

$$K = \sum_{i \in V} K_i$$

This method of estimation was originally proposed by Oda (1985).

A drawback of this approximation is that it generally overestimates the block-scale hydraulic conductivity that would be obtained by an explicit block-scale DFN calculation. Not all fractures within a given volume will form part of the conductive "backbone" of the through-flowing network, and network tortuosity further reduces the effective hydraulic conductivity. However this approximation can be calculated with much less computational effort than is required for the more rigorous approach of permeameter simulations (as described below).

Block-scale porosity is calculated as a scalar property:

$$\theta = \sum_{i \in V} \frac{b_i}{s_i} = \frac{1}{V} \sum_{i \in V} b_i A_i$$

where b_i is the effective transport aperture of the ith fracture. Note that this does not take into account possible directional dependence of block-scale porosity, nor network effects.

A geometrical estimate of flow-wetted surface is calculated as a scalar property:

$$a_r = \frac{2}{V} \sum_{i \in V} A_i$$

Note that this similarly does not take into account possible directional dependence of flow-wetted surface, nor network effects.

Depending on the goals of the simulation, geometrical estimates were produced either for all 6000 of the grid cells in the 6 km^3 volume:

X = 1 630 000 m to 1 633 000 m
Y = 6 699 000 m to 6 701 500 m
Z = -800 m to 0 m

with a cell size of $(100\text{ m})^3$, or for a random selection of 40 to 100 blocks from the same grid.

The latter approach was used in simulations where the fracture coordinates and properties were saved for permeameter simulations, so that geometric estimates could be compared directly with permeameter estimates. Due to the very large number of fractures in the full simulation volume, storing the fracture data for a full simulation was not practical.

The random selection of cells is done independently and randomly by an acceptance -rejection procedure to produce an unbiased sample of sites in 3-D. Figure 2.2 shows an example of the lateral and vertical distribution of cells that were sampled in one case.

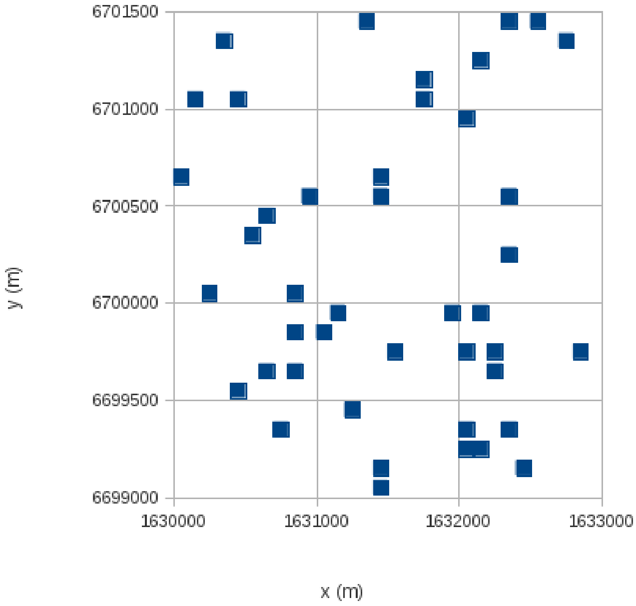

z (m)	N
-50	7
-150	5
-250	12
-350	5
-450	5
-550	6
-650	5
-750	4

Figure 2.2. Example of spatial distribution of sampled cells for combined geometric and permeameter estimation of rock mass hydraulic properties. Plot shows distribution of cell locations in plan view; table shows distribution in the vertical direction. The high proportion of cells at Z = -250 m in this example is an example of stochastic clustering; other realizations of the sampling scheme produced fewer cells in this depth range.

2.2.3. Permeameter estimates of rock hydraulic properties

Block-scale permeameter simulations, by explicit modeling of flow through a DFN network model, can provide estimates of the effective directional components of $\mathbf{K}$, as well as the estimates of the effective θ and a_r for a given flow direction. This approach accounts both for the finite size of fractures and connectivity effects on the block scale. It also provides a possibility to evaluate the applicability of the hydraulic conductivity tensor for a given block scale.

Methodologies for permeameter simulations to evaluate hydraulic conductivity tensors were investigated by Long *et al.* (1982) and subsequent authors. In the present study, a relatively simple methodology is used with simulations in just three orthogonal directions. This approach is intended as an initial analysis suitable for the current phase of review.

The procedure uses the same DFN simulations as for the geometric estimates, allowing direct comparison between methods. The fractures for a randomly selected subset of the blocks (as in Figure 2.2) are discretized within a cubical boundary to produce a finite-element mesh on the selected scale (20 m, 50 m, or 100 m), using the mesh-generation methods and algorithms of the DFM software (Geier, 2010).Flow simulations are then performed in each of the three orthogonal directions corresponding to the cubical boundary edges. A fixed head gradient is applied between the upstream and downstream ends of the cube, with linearly declining heads along the other boundaries (Figure 2.3). Effective directional hydraulic conductivities are calculated as the ratio of the flows to the applied head gradient, per unit cross-sectional area.

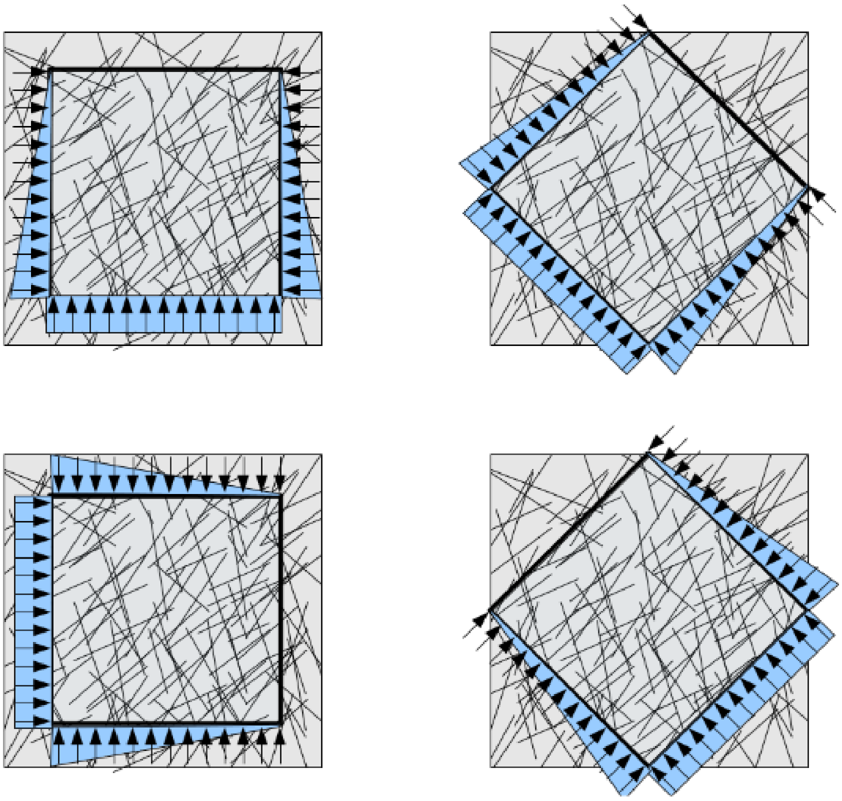

Figure 2.3. Schematic illustration of permeameter simulations with declining-head boundary conditions.

A more detailed analysis could consider additional directions for the applied gradient, to test for consistency of the directional conductivities with the assumption of a hydraulic conductivity tensor. Another possible refinement could be use of “guard zones” along the sides with declining-head boundary conditions, to reduce the effect of flows through fractures that happen to cut across a corner. These refinements were not used in the present study but could be considered in further investigations if warranted.

Flux-weighted estimates of θ, and a_r are produced from each directional flow simulation by integration over the calculated network flow fields. The estimates are weighted with respect to groundwater flux, so that the results represent primarily the pathways through each block (for the given direction of hydraulic gradient) that carry the bulk of the flow (generally less than the total fracture porosity and wetted surface, as obtained from the geometrical calculation methods described above).

Flux-weighted porosity for a head gradient parallel to the *i*th coordinate axis is calculated as a weighted sum over all finite elements in the block-scale mesh, either as:

$$\langle \theta_i \rangle_q = \frac{1}{V} \frac{\sum_{e \in V} q_e b_e A_e}{\sum_{e \in V} q_e}$$

$$\langle \theta_i \rangle_{qA} = \frac{1}{V} \frac{\sum_{e \in V} q_e b_e A_e^2}{\sum_{e \in V} q_e A_e}$$

where b_e is the effective transport aperture of the *e*th triangular finite element in the mesh, q_e is the magnitude of flux in that element, and A_e is its area. The first of these estimates emphasizes the elements that carry the highest fluxes, regardless of their size, while the second measure includes element area to reduce the tendency to skew results toward a few small elements that might have very high local fluxes.

Conceptually analogous flux-weighted estimates of flow-wetted surface are calculated as:

$$\langle a_{r_i} \rangle_q = \frac{2}{V} \frac{\sum_{e \in V} q_e A_e}{\sum_{e \in V} q_e}$$

$$\langle a_{r_i} \rangle_{qA} = \frac{2}{V} \frac{\sum_{e \in V} q_e A_e^2}{\sum_{e \in V} q_e A_e}$$

2.3. Interaction of natural fractures with EDZ

This issue is investigated by embedding a section of deposition tunnel within realizations of a block-scale DFN model, and simulating flow due to hydraulic gradients imposed parallel and perpendicular to the tunnel axis.

The tunnel is assumed to be backfilled, with either a continuous or discontinuous EDZ. Deposition holes are included to allow evaluation of fluxes to deposition holes, and advective-dispersive transport calculations as described below. The deposition holes positions are conditioned on the DFN realization to avoid fractures with full-perimeter intersections. The deposition holes are represented as vertical hexagonal prisms (Figure 2.4), following the methods of Geier (2011). Conditional placement of deposition holes for a given realization of the DFN is according to the FPC criterion of Munier (2010), as implemented in the DFM module *repository* (Geier, 2008). Parameters governing deposition hole geometry and placement along the tunnels are as listed in Table 2.3.

Locations of the blocks for these simulations are chosen randomly from the site-scale DFN model domain, but restricted to blocks that are centered at -450 m (as an approximation of the repository depth, to the nearest 100 m grid division).

While the location of the deposition holes can vary depending on the locations of large stochastic fractures, typically twelve deposition holes are simulated per 100 m block, after allowing space at both ends of the tunnel segment.

Four cases are considered for each block and tunnel segment:

- Continuous EDZ (all EDZ elements are retained with fixed transmissivity $T_{EDZ} = 10^{-8}$ m^2/s);
- 75% EDZ (25% of the EDZ elements are randomly assigned a very low transmissivity 10^{-5}xT_{EDZ}, so that flow will be focused in the remaining 75%);
- 50% EDZ (50% of the EDZ elements are randomly assigned a very low transmissivity 10^{-5}x$\mathrm{T}_{\mathrm{EDZ}}$, so that flow will be focused in the remaining 50%);
- No EDZ (all of the EDZ elements are assigned a very low transmissivity 10^{-5}xT_{EDZ}).

For each of these cases, flow fields are calculated by imposing an arbitrary but representative hydraulic gradient of 0.001 (on the order of the regional topographic gradient which is estimated as 0.00125; see Geier, 2012, Table 6.1), to drive flow in each of three orthogonal directions aligned with the cubical boundary: SW to NE (horizontal and parallel to the tunnel), SW to NE (horizontal and perpendicular to the tunnel), and vertically upward.

In each case and for each flow direction, an effective block-scale hydraulic conductivity is calculated as the mean flowrate divided by the cross-sectional area and the magnitude of the hydraulic gradient. Thus directional hydraulic conductivities are obtained in each of these three orthogonal directions (parallel and perpendicular to the tunnel, and vertical), for each of the cases of EDZ fractional continuity.

Table 2.3 Deposition hole parameters for the model.

	Parameter value	Justification
Deposition hole sides	6	Hexagonal approximation to circle
Deposition hole radius	0.88 m	SR-Can Initial State Report (SKB TR-06-21), Figure 5-3
Deposition hole depth	7.83 m	SR-Can Initial State Report (SKB TR-06-21), Figure 5-3
Canister radius	0.53 m	SR-Can Initial State Report (SKB TR-06-21), Figure 5-3
Canister length	4.83 m	SR-Can Initial State Report (SKB TR-06-21), Figure 5-3
Canister top	2.5 m	SR-Can Initial State Report (SKB TR-06-21), Figure 5-3
Distance between holes $L_{spacing}$	7.8 m	Based on D1 repository design (Brantberger et al., 2006)
Distance from drift end	20 m	Deep Repository, Underground Design Premises D1/1 (SKB R-04-60)
Distance from drift start L_{plug}	8 m	Deep Repository, Underground Design Premises D1/1 (SKB R-04-60)
Minimum step distance L_{step}	1 m	Assumed generic value
Pilot hole transmissivity	1×10^{-5} m^2/s	Assumed generic value

The flowrate to each deposition hole is calculated as the net flux crossing the deposition hole boundary. This corresponds to an open-hole condition rather than the case in which the hole is sealed with buffer. All deposition holes are intersected by the EDZ feature in the tunnel floor, and some are also intersected by stochastic fractures. Note that even in the “no EDZ” case, an EDZ feature of very low transmissivity intersects each deposition hole, though the groundwater flux may be negligible.

Flows to canister positions are calculated as the sum of all positive flows into the deposition hole (generally balanced by outflows).

The water velocity in the fractures intersecting the deposition holes is of interest for bentonite erosion modeling as well as for radionuclide transport. The mean velocity at the *i*th deposition hole was calculated as:

$$\bar{v}_i = \frac{\sum_{j\in i} Q_j}{\sum_{j\in i} L_j \, b_{Tj}}$$

where:

Q_j = flowrate across the *j*th element edge [L^3/T],

L_j = length of *j*th edge, and

b_{Tj} = transport aperture at *j*th edge.

and where the sums are taken over all element edges *j* that intersect the *i*th deposition hole.

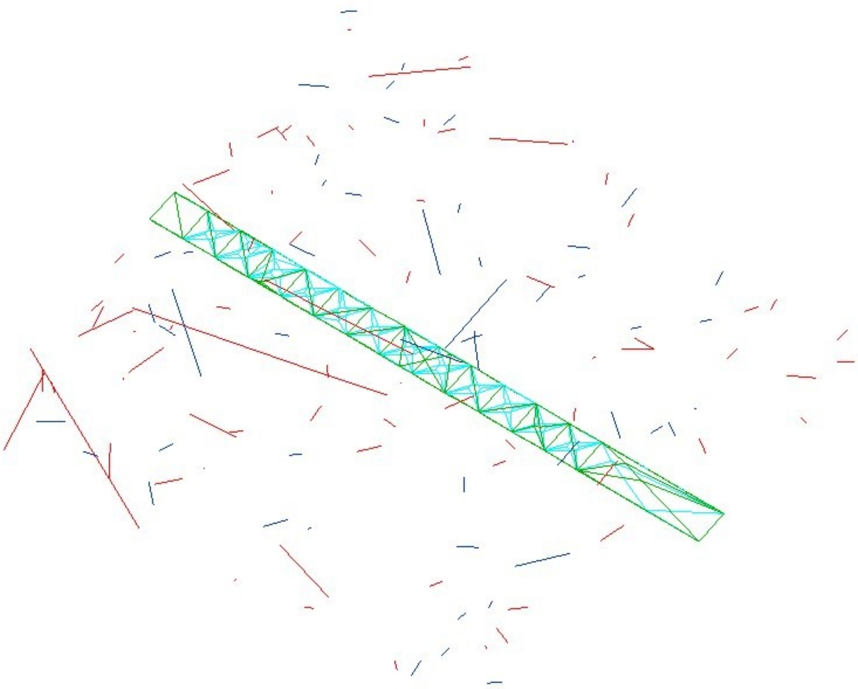

Figure 2.4. Plan view of finite-element mesh for the EDZ and deposition holes along a 100 m long tunnel segment, oriented from SE to NW, for the investigation of EDZ interactions with natural fractures along deposition tunnels. Green line segments indicate the boundaries of triangular finite elements along the roof of the tunnel. Blue/aqua line segments are element boundaries for the EDZ in the floor of the tunnel, with the deposition holes appearing as small hexagons in this view. Dark red and dark blue lines represent intersections of the DFN fractures with the upper and lower faces (at -400 m and -500 m, respectively) of the 100 m cube that is used as the boundary for flow simulations to evaluate EDZ properties. Note that these are just a small fraction of the discrete fractures that are contained entirely or partly within the cube. However, the sparseness of these intersections on the upper and lower faces is indicative of the sparseness of the DFN model at repository depths.

Advective-dispersive particle tracking is used to characterize transport properties of paths from deposition holes through the rock mass and/or EDZ. This yields estimates of water residence times t_w, path lengths L, and transport resistance F for paths via the EDZ and/or the stochastic DFN on scales up to 100 m. The scale of 100 m is a representative value for transport via the EDZ and rock mass before reaching a hydraulically conductive, site-scale deformation zone; for example, in Figure 3-10 of Selroos and Follin (2009) it may be seen that nearly all deposition holes locations are within 400 m of the nearest deterministic deformation zones, most are within 200 m, and many are so close that the computational grid cell containing the deposition hole is also intersected by a deformation zone.

Advective-dispersive transport of non-sorbing solute through the 3-D network (neglecting matrix diffusion) is modelled by the discrete-parcel random walk method (Ahlstrom et al., 1977). This approach represents local, 2-D advective-dispersive transport within each fracture plane. 3-D network dispersion, due to the interconnectivity among discrete features, arises as the result of local dispersion in combination with mixing across fracture intersections.

For mathematical details and definition of parameters see Geier (2005; 2008b). The algorithm assumes complete mixing at fracture intersections; this is a reasonable approximation for the low advective flow velocities expected in a post-closure repository, as discussed by Geier (2008a).

Particles are initiated from source locations, which in the present study comprise the intersections of transmissive features with the perimeters of the deposition holes. For each canister position that is intersected by a transmissive feature, 100 particles are released. Transport parameters used in this step are summarized in Table 2.4.

Table 2.4 Parameters for advective-dispersive particle tracking.

Parameter	Feature Category	Feature Set(s)	Value
Molecular diffusion coefficient	All	All	$2.0\text{x}10^{-9}$ m^2/s
Ratio of transverse dispersivity to longitudinal dispersivity	All	All	0.1
Longitudinal dispersivity	Repository tunnels	1	1 m
	Single fractures	> 1	1 m

2.4. Sensitivity of fracture hydraulic properties to future stress conditions

The sensitivity of rock-mass hydraulic properties to future stress conditions is investigated by calculating block-scale geometrical estimates of rock mass hydraulic conductivity and porosity (**K** and θ) due to predicted changes in effective rock stresses during future glaciations.

The method makes use of the relation between fracture normal stress and mechanical aperture as defined in SR-Site (TR-11-01 p 333, Figure 10-20, based on Hökmark Figure 4-9):

$$e = e_r + e_{max} e^{-\alpha\sigma_n}$$

It is assumed that the fracture transmissivities simulated in each realisation of the DFN model are representative of the present-day stress conditions at their respective depths. By calculating the normal stress σ_n as resolved on the given fracture plane at the given depth, based on the SR-Site model for vertical and principal horizontal stresses as functions of depth, and the corresponding normal stress σ_n' for a given future state of stress, the ratio of the future and present mechanical aperture is obtained from:

$$\frac{e'}{e} = \frac{e_r + e_{max} e^{-\alpha\sigma_n'}}{e_r + e_{max} e^{-\alpha\sigma_n}}$$

It is further assumed that transmissivity scales as the cube of mechanical aperture. On this basis the fracture transmissivity under the future state of stress is:

$$T' = T\left(\frac{e'}{e}\right)^3$$

which can be used as the basis for block-scale geometrical calculations as described in Section 2.2.2. based on summing the contributions of individual fractures, after applying fracture normal stress vs. transmissivity models as described in the SR-Site data report.

Note that this approach does not account for connectivity or coupled stress-flow effects. It is intended only to provide a means for scoping changes in bulk hydraulic properties of the bedrock due to glacial loading.

The basic method for making these calculations was developed and implemented in the course of this modelling project. However, results are not presented due to lack of well-defined stress functions for future glacial loading states, and prioritization of other parts of the modeling project.

2.5. Site-scale model development

A multi-scale discrete-feature model for the Forsmark site was developed based on modifications of a previous implementation by Geier (2010; 2011).Key modifications to the previous model included the following:

- Shallow bedrock aquifer features trimmed to portions SSW of ZFMWNW0001 and NNW of ZFMENE0062A
- Equivalent features (K-lattice): Added vertical cell boundary at -468 m (deposition tunnel floor level) and shifted -420 m and -520 m levels to -448 m and -488 m so K values reflect only deleted fractures within 20 m of tunnels (as shown schematically in Figure 2.5);
- Repository: Includes vertical shafts (“generic” location due to restrictions on coordinates) and inclined access ramp with multiple sections for different sealing methods per TR 11-01 Figure 5-25.
- EDZ transmissivity in deposition tunnels is 10^{-8} m^2/s per TR-11-01, p. 295.
- EFPC criterion for the Hydro-DFN now applies to any intersections with deposition hole (per TR-11-01, p. 152);
- Maximum transmissivity of deposition holes 10^{-10} m^2/s (integrated along length of deposition hole and averaged around wall, TR-11-01, p. 150); this constraint is applied post-simulation by identifying deposition holes that exceed this value.

Due to time constraints and prioritization of other aspects of this modeling project, only a few trial flow simulations of the revised site-scale model were attempted. These did not converge to adequately accurate solutions of the flow equations to provide reliable results for this project. Therefore a detailed explanation of the refined model is omitted from this technical note.

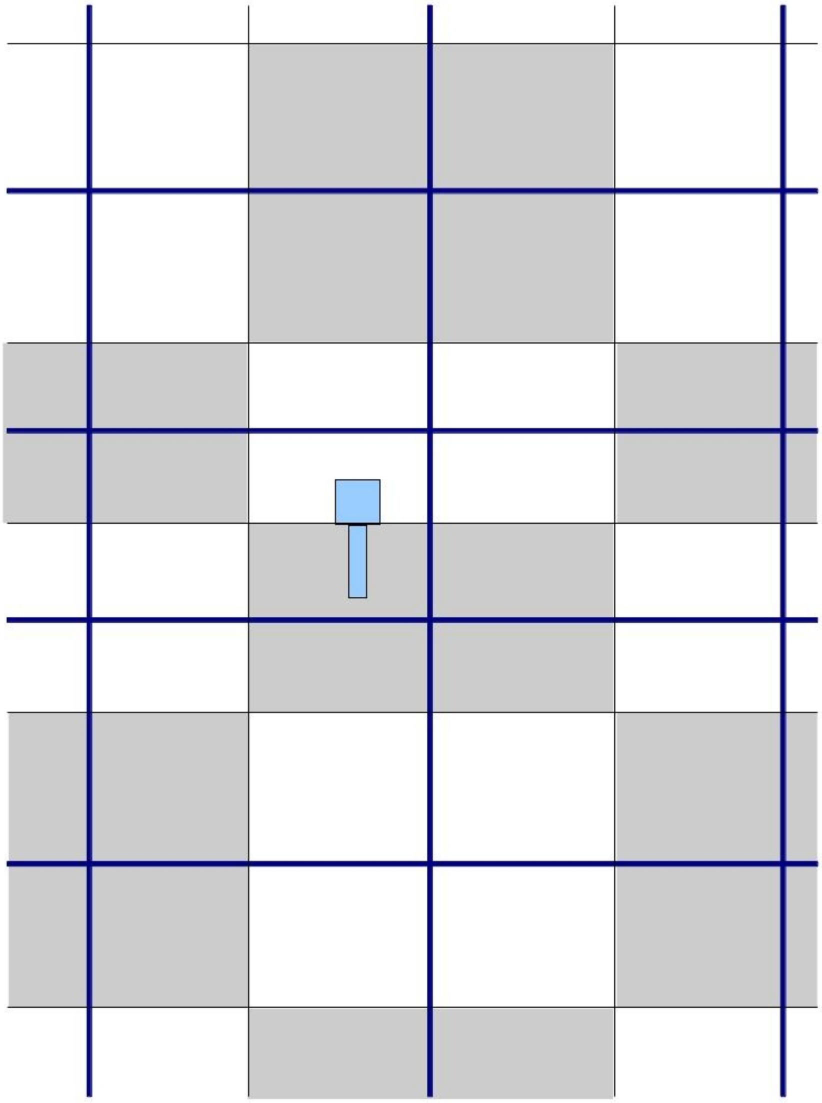

Figure 2.5. Schematic illustration of design of grid cells and equivalent-continuum features to avoid artefacts of these features intersecting deposition holes. Shaded gray and white areas represent grid blocks; blue lines indicate schematic locations of equivalent features to represent the effective hydraulic conductivity of the grid blocks.

3. Results and Analysis

3.1. Estimation of effective continuum properties

Equivalent continuum properties **K**, θ, and a_r for the rock mass were obtained by three methods, as detailed in Section 2.2:

- Analytical/semi-analytical estimates;
- Block-scale DFN geometrical calculations based on summing the contributions of individual fractures;
- Block-scale DFN flow (permeameter) simulations to calculate effective directional components of **K**, and flux-weighted estimates of θ, and a_r.;

The results of these calculations are presented in the following subsections.

3.1.1. Analytical estimates of rock hydraulic properties

The analytical expressions for rock mass hydraulic properties, as given in Section 2.2.1, require suitable average values of fracture transmissivity and transport aperture, for each fracture set and domain. Due to the complicated density functions for these variables, and correlations with fracture radius (and thus fracture area) which are implicit in the semi-correlated model for fracture transmissivity, stochastic simulation was used to obtain appropriate estimates.

The results for Fracture Domain FFM01 are listed in Table 3.1. Equivalent results were obtained for the other fracture domains, but are omitted here for the sake of space, and because FFM01 is the domain of primary interest for flow within the proposed repository.

Using these values, the analytical formulae in Section 2.2.1 were applied to obtain estimates of the hydraulic conductivity tensors, porosity, and flow wetted surface for each fracture domain and depth subdomain. These results are summarized in Table 3.2. The full **K** tensors including off-diagonal components are listed in Table 3.3.

Domain	Depth Sub-domain	Fracture Set	Mean Transmissivity (m^2/s)		Mean Aperture (m)	
			Unweighted	Weighted by fracture area	Unweighted	Weighted by fracture area
FFM01	shallow	1	1.55E-06	9.58E-06	4.03E-04	1.22E-03
FFM01	shallow	2	6.09E-07	1.13E-05	2.51E-04	8.67E-04
FFM01	shallow	3	1.14E-06	1.52E-06	3.81E-04	4.67E-04
FFM01	shallow	4	5.23E-07	2.97E-06	2.37E-04	4.58E-04
FFM01	shallow	5	1.58E-06	2.03E-05	3.96E-04	1.28E-03
FFM01	middle	1	9.36E-09	3.23E-08	3.29E-05	5.97E-05
FFM01	middle	2	1.28E-08	3.35E-08	3.86E-05	5.75E-05
FFM01	middle	3	8.82E-09	1.38E-08	3.19E-05	3.80E-05
FFM01	middle	4	1.23E-08	2.30E-08	3.69E-05	4.33E-05
FFM01	middle	5	9.56E-09	5.78E-08	3.32E-05	7.55E-05
FFM01	deep	1	5.13E-10	6.12E-10	7.64E-06	9.26E-06
FFM01	deep	2	3.78E-10	1.52E-09	6.66E-06	1.23E-05
FFM01	deep	3	4.73E-10	7.00E-10	7.54E-06	9.08E-06
FFM01	deep	4	3.58E-10	7.51E-10	6.48E-06	8.79E-06
FFM01	deep	5	5.20E-10	8.61E-10	7.78E-06	1.09E-05

Table 3.1 Mean transmissivities and mean apertures calculated from multiple simulations (total of 4,752,520 fractures), for fracture domain FFM01. Equivalent estimates were obtained for the other fracture domains but are omitted for the sake of space.

Domain	Subdomain	Hydraulic Conductivity Tensor Components			Porosity	Wetted Surface a_r (1/m)
		K_{11} (m/s)	K_{22} (m/s)	K_{33} (m/s)		
FFM01	**deep**	**2.15e-08**	**3.32e-08**	**4.20e-08**	**5.64E-06**	**1.07**
FFM01	**middle**	**5.01e-07**	**5.62e-07**	**7.27e-07**	**6.07E-05**	**2.03**
FFM01	**shallow**	**1.85e-04**	**9.82e-05**	**2.08e-04**	**1.16E-03**	**2.30**
FFM02	**shallow**	**1.83e-06**	**2.44e-06**	**3.40e-06**	**6.49E-04**	**6.33**
FFM03	**deep**	**1.67e-06**	**2.49e-06**	**3.36e-06**	**3.79E-05**	**1.54**
FFM03	**shallow**	**4.60e-06**	**4.21e-06**	**7.08e-06**	**1.93E-04**	**2.19**

Table 3.2 Summary of analytical estimates of rock mass hydraulic properties.

Domain	**Subdomain**	**Hydraulic Conductivity Tensor Components K_{ij} (m/s)**		
FFM01	**deep**	**2.146E-08**	**2.316E-09**	**-2.553E-10**
		2.316E-09	**3.319E-08**	**3.794E-10**
		-2.553E-10	**3.794E-10**	**4.203E-08**
FFM01	**middle**	**5.011E-07**	**5.637E-08**	**-1.554E-08**
		5.637E-08	**5.622E-07**	**5.091E-09**
		-1.554E-08	**5.091E-09**	**7.271E-07**
FFM01	**shallow**	**1.854E-04**	**8.954E-07**	**-3.120E-06**
		8.954E-07	**9.823E-05**	**4.044E-06**
		-3.120E-06	**4.044E-06**	**2.084E-04**
FFM02	**shallow**	**1.828E-06**	**1.454E-07**	**-6.872E-09**
		1.454E-07	**2.436E-06**	**3.689E-08**
		-6.872E-09	**3.689E-08**	**3.402E-06**
FFM03	**deep**	**1.672E-06**	**4.818E-07**	**-2.366E-08**
		4.818E-07	**2.487E-06**	**3.144E-08**
		-2.366E-08	**3.144E-08**	**3.360E-06**
FFM03	**shallow**	**4.604E-06**	**3.393E-07**	**-2.657E-08**
		3.393E-07	**4.210E-06**	**9.858E-08**
		-2.657E-08	**9.858E-08**	**7.075E-06**

Table 3.3 Analytical estimates of rock mass hydraulic conductivity tensor components.

3.1.2. Geometrical estimates of rock hydraulic properties

Geometrical estimates of scale rock hydraulic properties are shown in Figures 3.1 through 3.3, for hydraulic conductivity, porosity, and flow-wetted surface respectively. The analytical estimates for the different depth intervals of fracture domain FFM01 are shown as red lines for comparison.

The geometrical estimates of block-scale hydraulic conductivity are mostly lower than the analytical estimates, particularly for the smaller 50 m block scale (Figure 3.1). Similarly, the geometrical estimates of porosity and flow-wetted surface (Figures 3.2 and 3.3) tend to be lower than the analytical estimates. However, heterogeneous distribution of fractures arising from the stochastic simulation gives rise to many blocks with lower estimated values, and a few blocks with higher estimated values of these properties.

A possible explanation for the closer agreement between the geometrical and analytical estimates on the 100 m block scale may be that the larger blocks tend to be dominated by a few large fractures. These large fractures tend to be significantly more transmissive, because of the semi-correlated relationship between fracture size and fracture transmissivity *T*. This affects the hydraulic conductivity distribution most strongly due to the linear relationship between *T* and **K**, but also carries into the porosity estimates due to the assumed proportionality of transport aperture to the square root of *T*.

Geometrical estimates of flow-wetted surface show a weak correlation to hydraulic conductivity (Figure 3.4). A correlation in these estimates is expected because blocks with more fractures (and hence more fracture surface area per unit volume) tend to have higher hydraulic conductivity. The weakness of the correlation may be due to the strong effect of large, high-transmissivity fractures which contribute to the **K** tensors in proportion to the product of *T* times area, but contribute to the wetted surface estimates only in proportion to their area.

A bimodality is apparent in the results for hydraulic conductivity (Figure 3.1), particularly at depths below Z = -300 m. Comparison with a larger set of geometric estimates from a single realization (Figure 3.5) shows that this bimodality persists and becomes more clear in the larger simulated data set.

Cross-sections of geometrical estimates for the full set of grid cells (Figures 3.6 through 3.8) show that the bimodality arises from different parts of the simulated domain, corresponding to the different fracture domains. Distinctly lower *K* values (visible as the dark green area in the cross-sections from Z = -450 m and deeper) are found within fracture domain FFM01 (i.e. inside the “tectonic lens”) at depth, compared with the outer fracture domains.

At shallower depths this bimodal pattern is reversed, with higher *K* values in the inner part of the domain (visible as yellow to orange cells), and lower *K* values outside this.

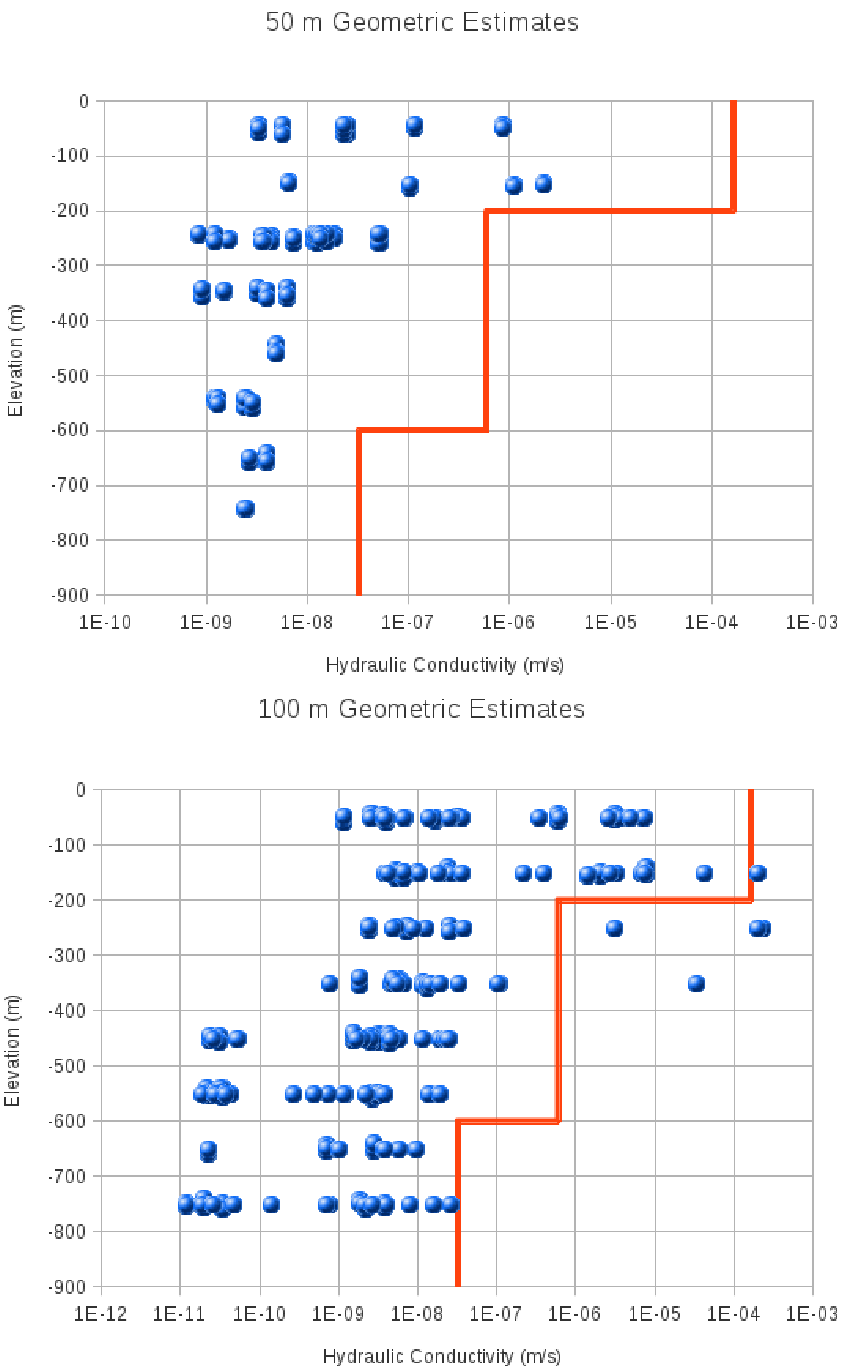

Figure 3.1. Geometrical estimates of hydraulic conductivity versus depth for (a) 50 m and (b) 100 m block scales, plotted as the mean (K_x+K_y+K_z)/3. The red line in each plot shows the corresponding analytical estimate of hydraulic conductivity for FFM01, depending on depth. Results shown are for a single realization in which fracture data were saved for randomly selected grid cells, for comparison with permeameter simulations.

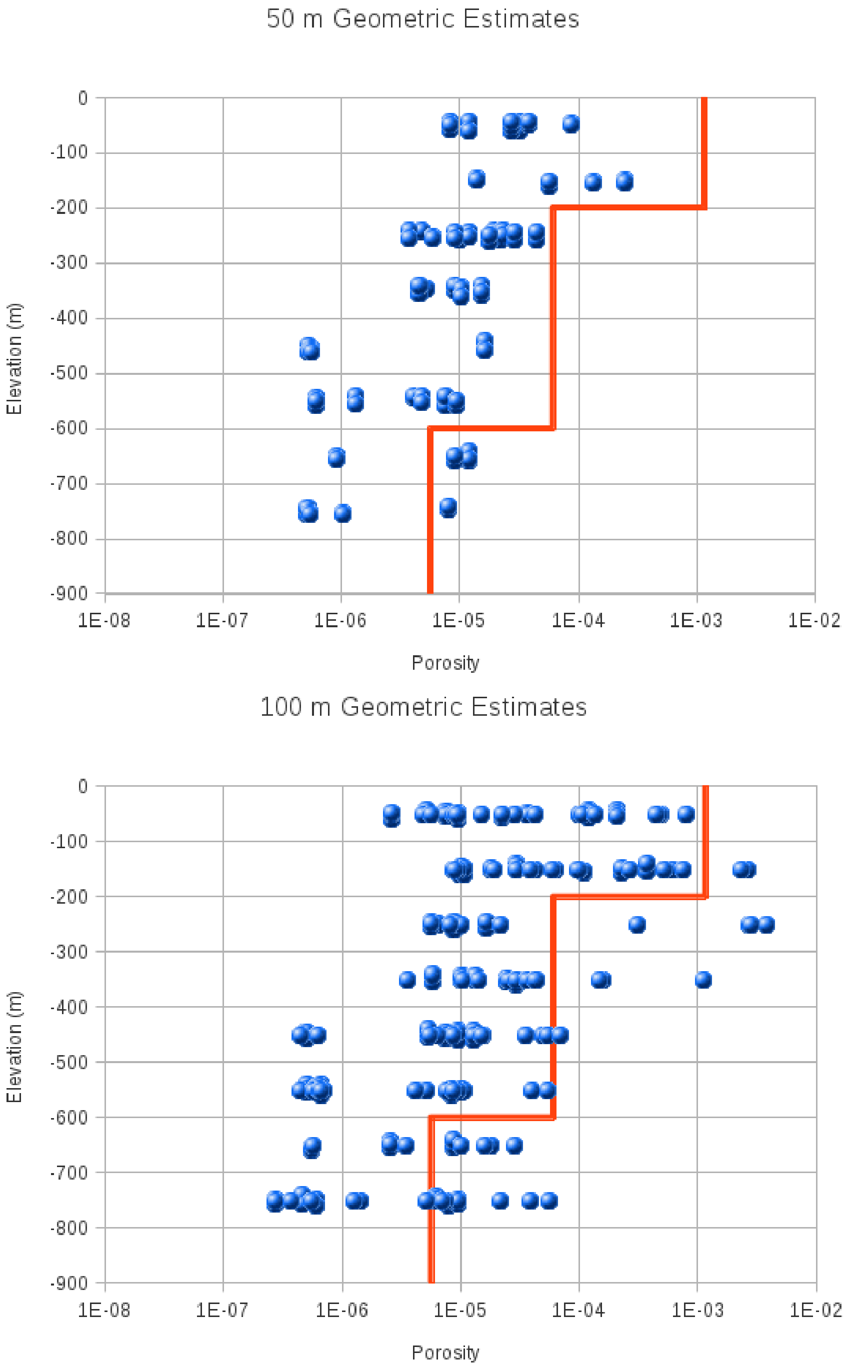

Figure 3.2. Geometrical estimates of porosity versus depth for (a) 50 m and (b) 100 m block scales. The red line in each plot shows the corresponding analytical estimate of hydraulic conductivity for FFM01, depending on depth. Results are for the same realization and sampling of grid cells as in Figure 3.1.

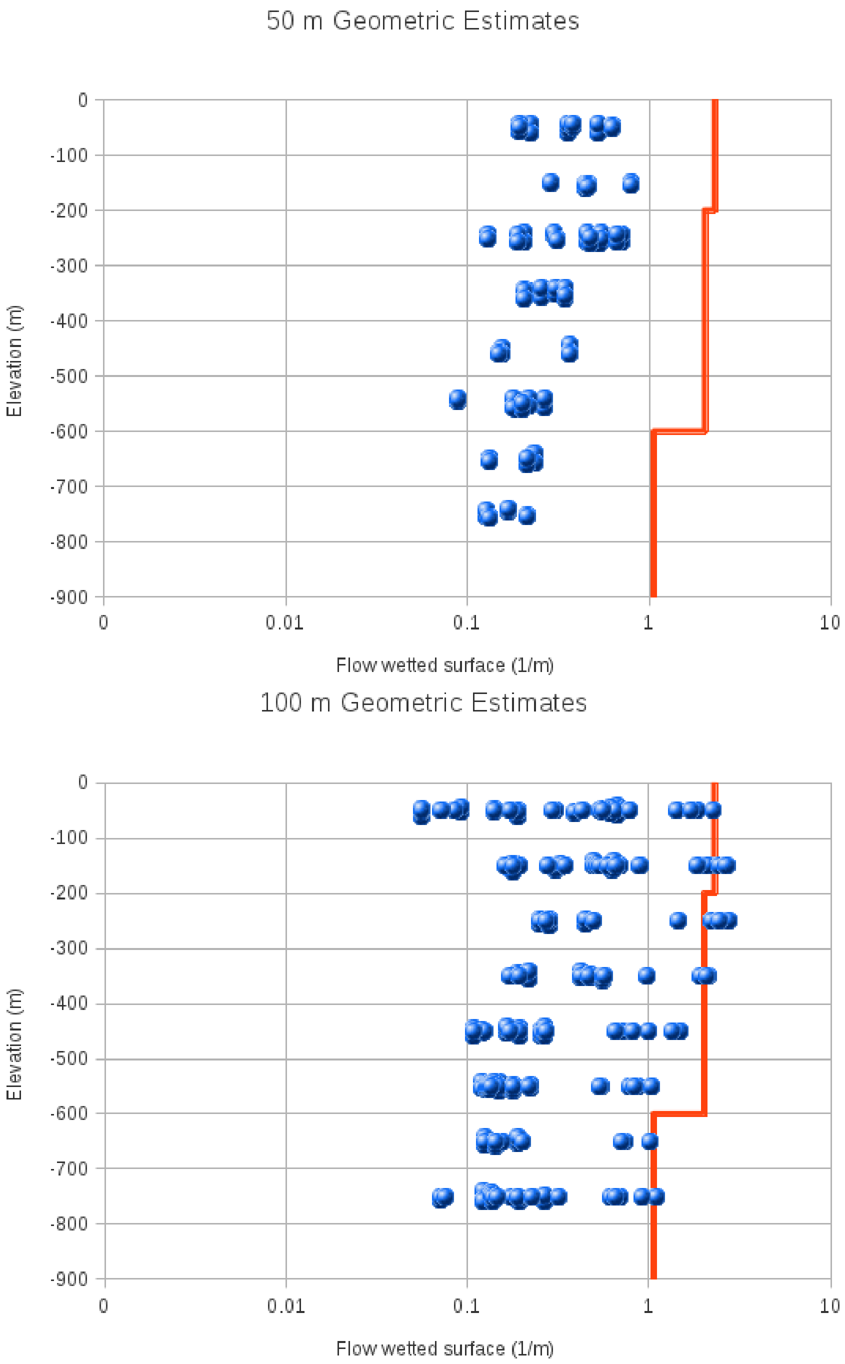

Figure 3.3. Geometrical estimates of flow-wetted surface versus depth for (a) 50 m and (b) 100 m block scales. The red line in each plot shows the corresponding analytical estimate of hydraulic conductivity for FFM01, depending on depth. Results are for the same realization and sampling of grid cells as in Figure 3.1.

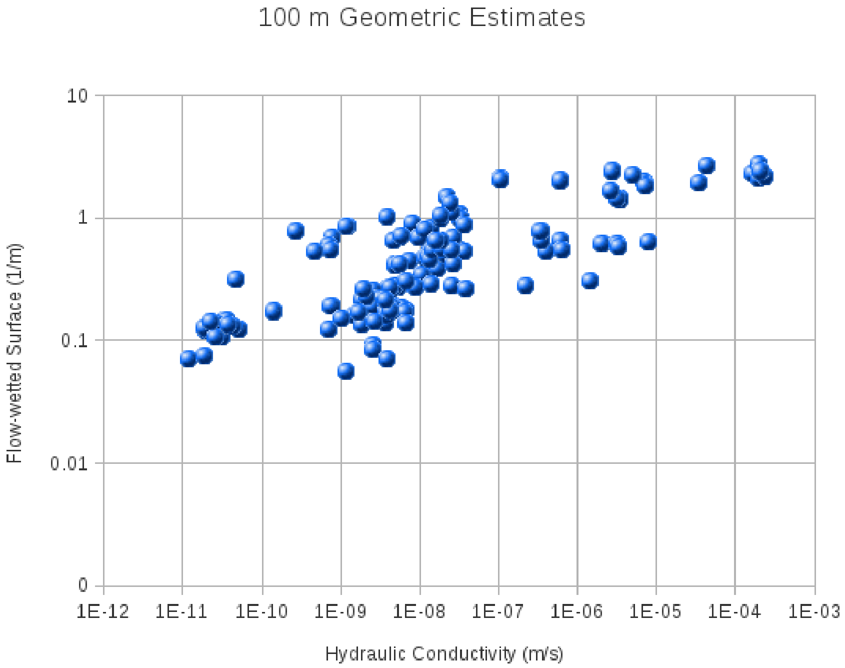

Figure 3.4. Geometrical estimates of flow-wetted surface versus hydraulic conductivity for the 100 m block scale. Results are for the same realization and sampling of grid cells as in Figure 3.1.

Thus the DFN model for Forsmark is found to produce contrastingly high conductivity in the shallow part of the "tectonic lens." This effect is in addition to the the "shallow bedrock aquifer" which is included explicitly in the Site Descriptive Model for hydrogeology. The estimated hydraulic conductivity tensors throughout the model are dominantly horizontal (Figure 3.9).

Together with the generally elevated *K* values at shallow depths, the horizontal anisotropy of the DFN model can be expected to produce predictions of site-scale groundwater flow in which flow is focused through the upper part of the "tectonic lens." Thus the geometrical properties of the DFN lead to a result that is is consistent with this key aspect of SKB's site interpretation.

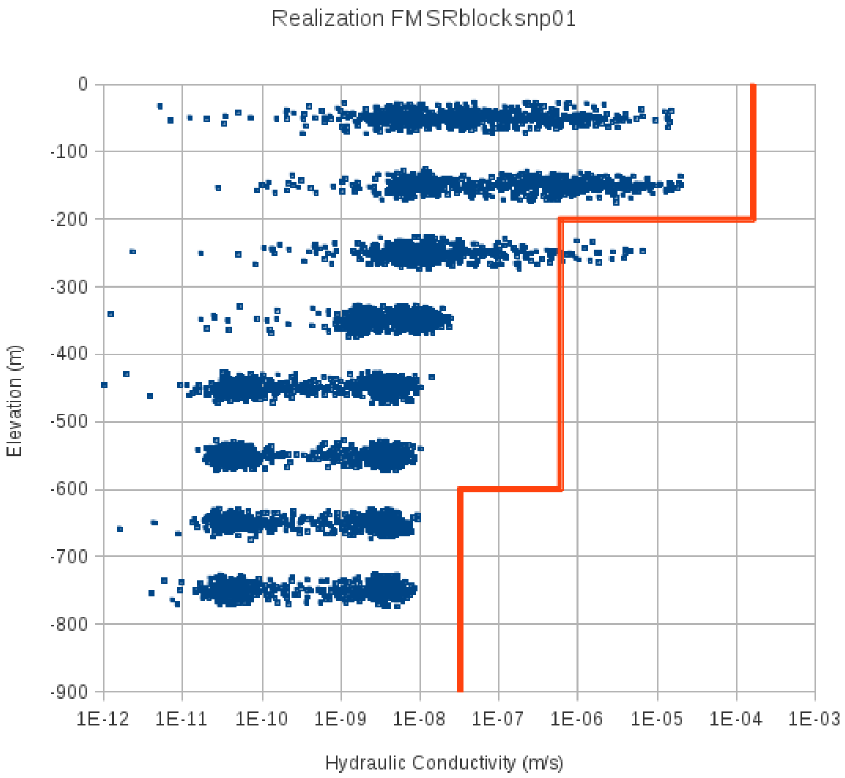

Figure 3.5. Geometrical estimates of hydraulic conductivity versus depth (negative elevation Z) for 100 m block scales, plotted as the mean $(K_x+K_y+K_z)/3$. The red line in each plot shows the corresponding analytical estimate of hydraulic conductivity for FFM01, depending on depth. Results shown are for a single realization in which geometrical estimates of hydraulic conductivity were calculated for all grid cells. A random perturbation δZ, with $|\delta Z| \leq 25$ m, has been added to the Z coordinate as a visualization aid to show where results are more strongly clustered; the actual grid cell centers are all at exactly $Z = 50$ m – n(100 m) where $n = 1, 2, \ldots, 8$.

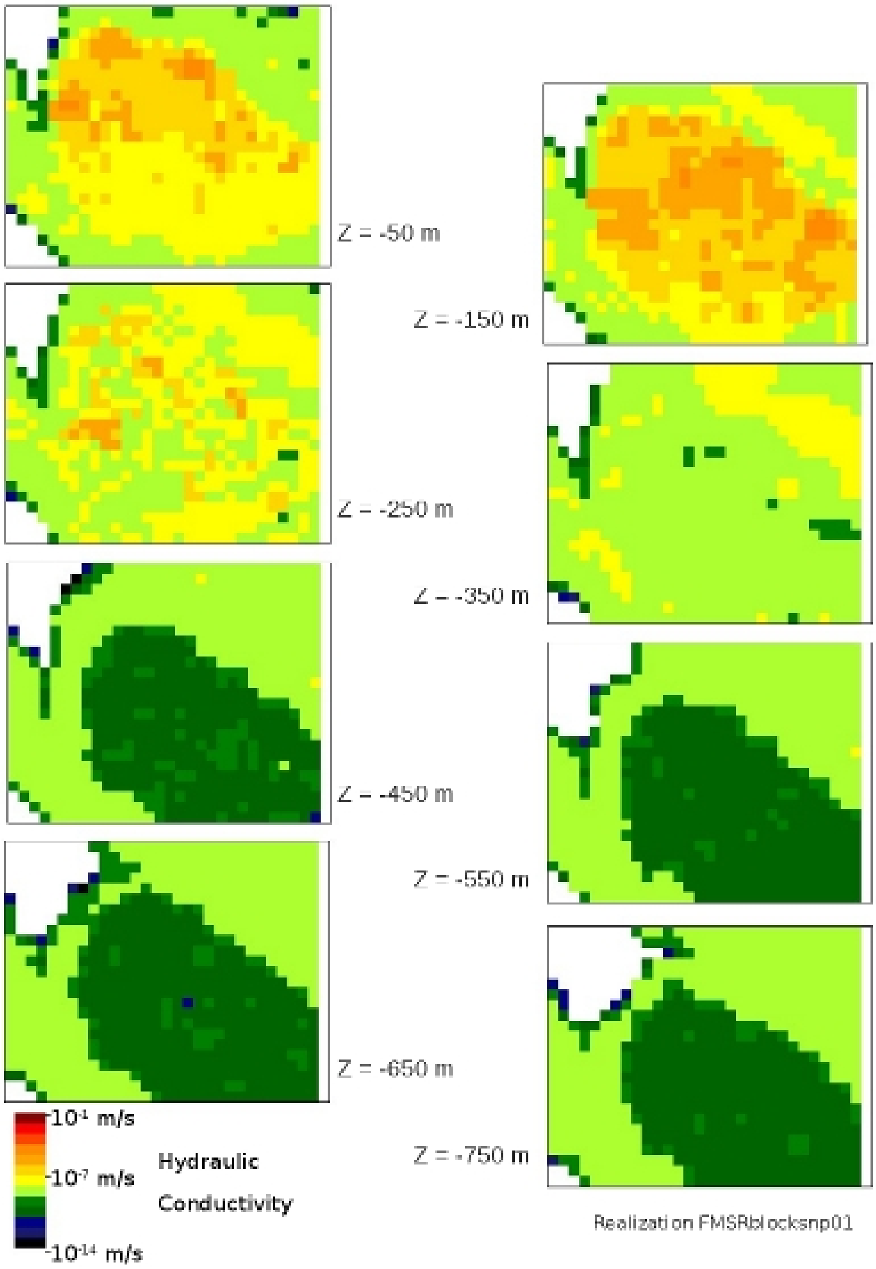

Figure 3.6 Cross-sections showing geometrical estimates of DFN hydraulic conductivity at depths ranging from -50 m to -750 (right column), for a single realization of the DFN model (FMSRblocksnp01). The color scale ranges from 10^{-14} m/s (dark blue/black) to 10^{-1} m/s (dark red). Blank (white) areas are outside of the defined fracture domains. The rectangular area shown is bounded by the coordinate ranges (x,y) = (1 630 000 m, 6 699 000 m) to (1 633 000 m, 6 701 500 m).

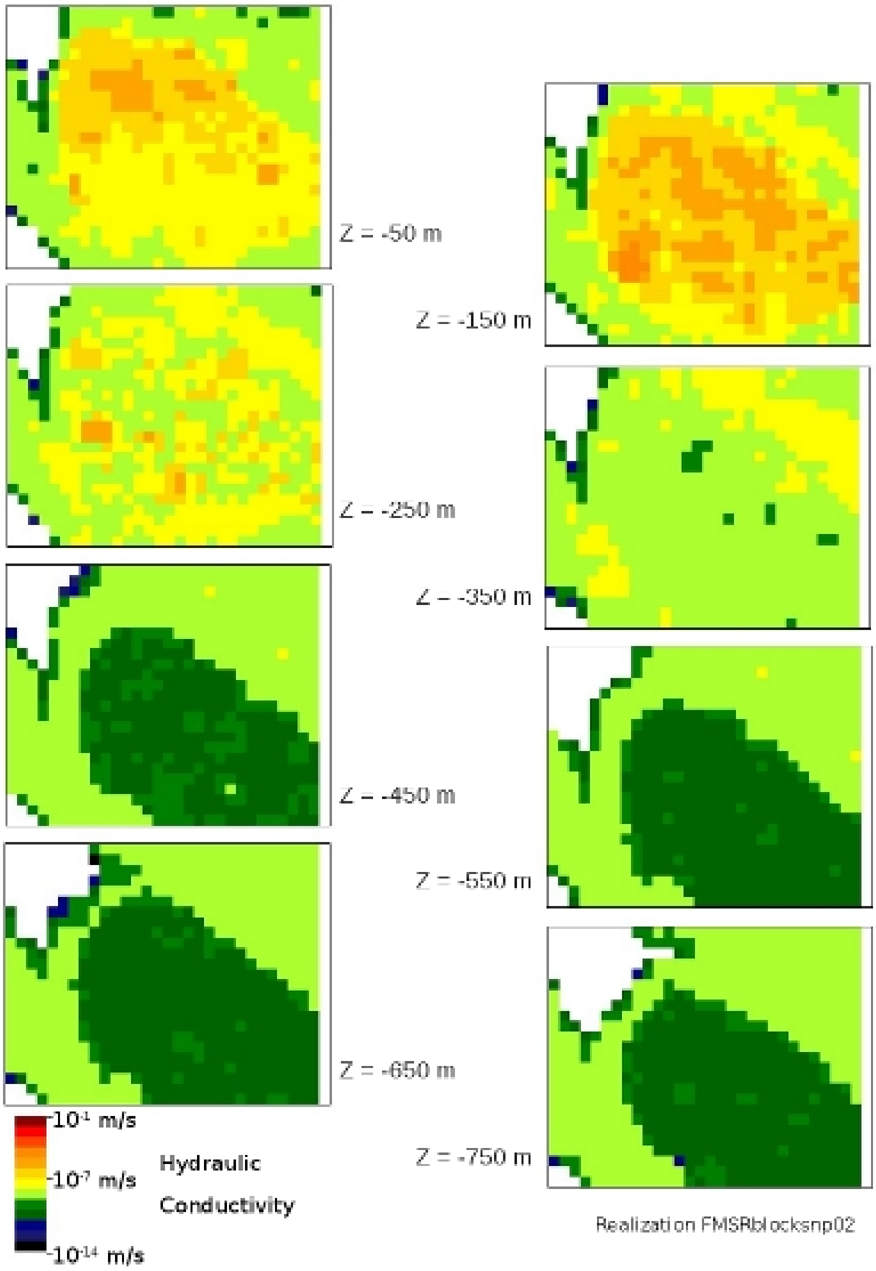

Figure 3.7 Cross-sections showing geometrical estimates of DFN hydraulic conductivity at depths ranging from -50 m to -750 (right column), for a single realization of the DFN model (FMSRblocksnp02). The color scale ranges from 10^{-14} m/s (dark blue/black) to 10^{-1} m/s (dark red). Blank (white) areas are outside of the defined fracture domains. The rectangular area shown is bounded by the coordinate ranges (x,y) = (1 630 000 m, 6 699 000 m) to (1 633 000 m, 6 701 500 m).

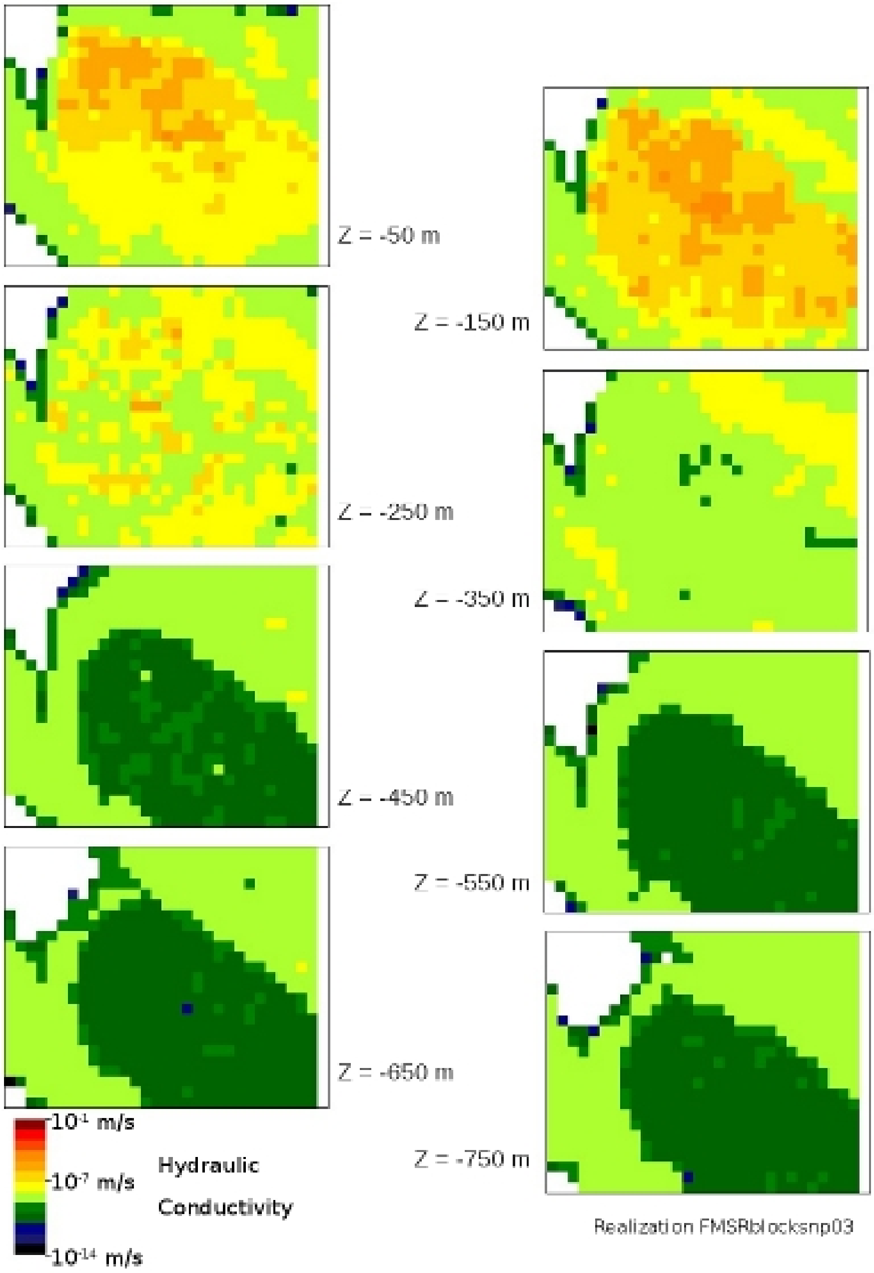

Figure 3.8 Cross-sections showing geometrical estimates of DFN hydraulic conductivity at depths ranging from -50 m to -750 (right column), for a single realization of the DFN model (FMSRblocksnp03). The color scale ranges from 10^{-14} m/s (dark blue/black) to 10^{-1} m/s (dark red). Blank (white) areas are outside of the defined fracture domains. The rectangular area shown is bounded by the coordinate ranges (x,y) = (1 630 000 m, 6 699 000 m) to (1 633 000 m, 6 701 500 m).

The geometrical estimates are produced at relatively low computational costs compared with permeameter estimates (which are presented in Section 3.1.3). The geometrical estimates give an indication of block-scale variability, which is not available from the single value that is produced by the analytical formulae. Thus this method provides a relatively simple way to produce synthetic fields of hydraulic properties (**K** tensors and porosities) for input to groundwater flow models based on continuum concepts. However some limitations of the method are apparent from further examination of the results.

Plots of anisotropy ratios based on geometric estimates of the tensor components (Figure 3.9) show that this method produces block-scale tensors with a limited degree of anisotropy. All of the anisotropy ratios plot within a triangular area with corners at the points corresponding to the cases:

$$K = \begin{bmatrix} K_x & 0 & 0 \\ 0 & (K_y = K_x) & 0 \\ 0 & 0 & 0 \end{bmatrix}$$

$$K = \begin{bmatrix} K_x & 0 & 0 \\ 0 & 0 & 0 \\ 0 & 0 & (K_z = K_x) \end{bmatrix}$$

$$K = \begin{bmatrix} 0 & 0 & 0 \\ 0 & K_y & 0 \\ 0 & 0 & (K_z = K_y) \end{bmatrix}$$

For blocks that are dominantly conductive in the horizontal plane (plotting close to the lower edge of this graph), the ratio of K_x to K_y is constrained to be approximately 1:1 (horizontally isotropic). Similarly, for blocks with dominantly vertical hydraulic conductivity, the conductivity is constrained to be approximately isotropic within that plane. Apparently this approach cannot generate **K** tensors that are dominated by hydraulic conductivity in a single, linear direction, for example cases such as $K_x >> K_y >> K_z$.

This results from the fact that the fractures in the DFN model are equidimensional (idealized as circular disks which are approximated by regular polygons which are squares in the CONNECTFLOW software used by SKB, or hexagons in the DFM software used here). From consideration of the equations in Section 2.2.2 which are the basis for the geometrical estimates, it can be shown that an equidimensional fracture will always contribute tensor components which are isotropic in the plane of the fracture.

The geometrical method could produce more strongly unidirectional **K** tensors, if applied to a DFN model with non-equidimensional fractures. However, DFN models with non-equidimensional fractures have not been presented in SKB's site descriptive model. As shown in the following section, the presented DFN models can produce stronger directional anisotropy due to connectivity effects which are accounted for in permeameter simulations, but not by the geometrical estimation method.

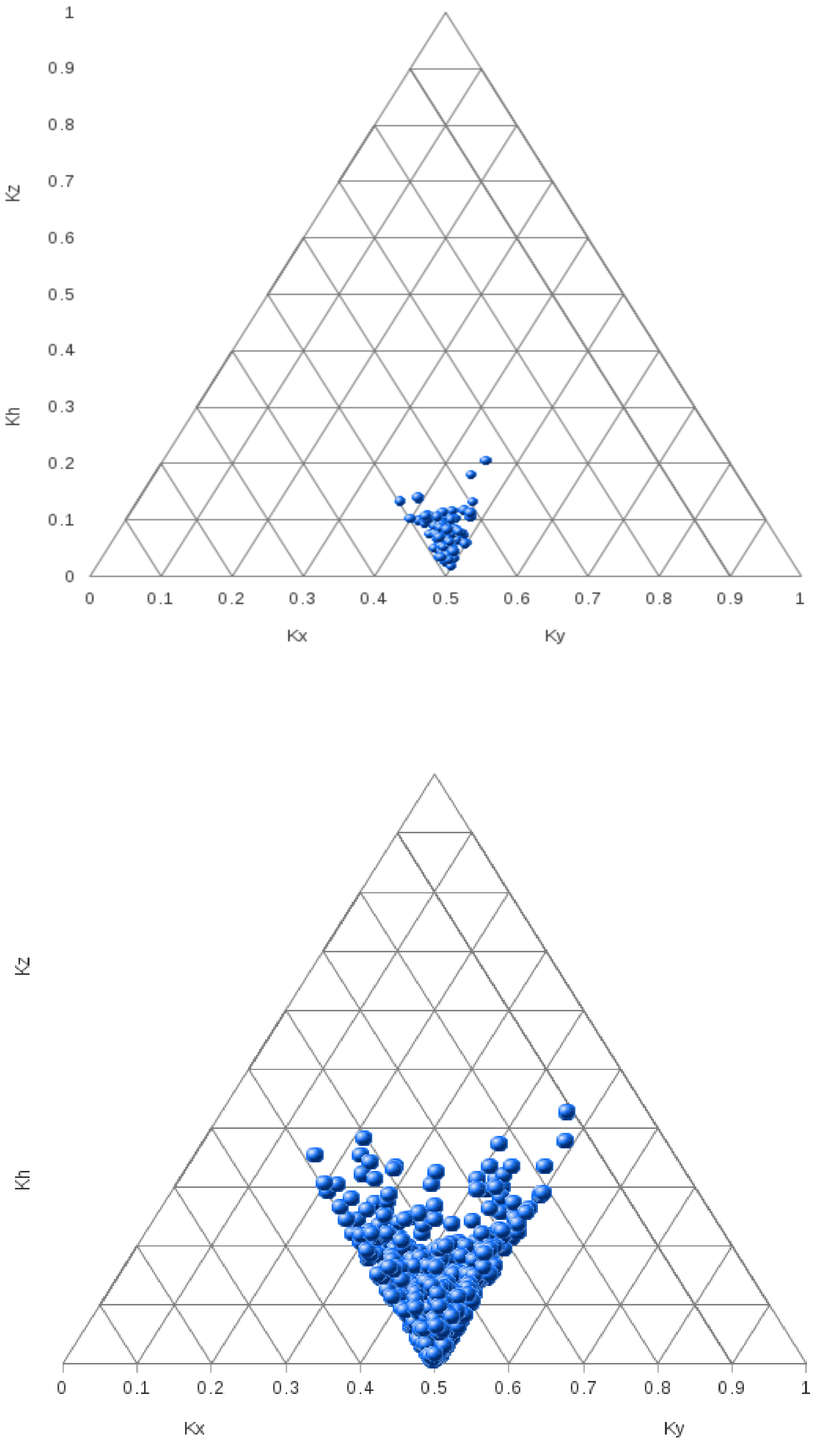

Figure 3.9 Anisotropy ratios for block-scale hydraulic conductivity tensors estimated by geometrical calculations from DFN simulations for (a) sample of 142 blocks, all depths and (b) larger sample of 1111 blocks, Z > -300 m. The horizontal grid lines represent equal ratios of vertical vs. horizontal conductivity. The grid lines that slope downward toward the right represent equal ratios of K_x versus conductivity in the *Y-Z* plane. The grid lines that slope upward toward the right represent equal ratios of K_y versus conductivity in the *X-Z* plane.

3.1.3. Permeameter estimates of rock hydraulic properties

Permeameter simulations were performed to estimate effective hydraulic conductivities in the three coordinate directions, for comparison to the geometric estimates for the same sample of grid-cell locations and DFN realizations. The permeameter simulations, using flow simulations on finite-element meshes that explicitly represent the complex geometry of interconnections among fractures, account for the effects of irregular connectivity as well as tortuosity of fracture flow paths

The results for one realization of the 50 m block scale and two realizations of the 100 m block scale are plotted in Figures 3.10 and 3.11, respectively. The general pattern seen is that the geometrical method overestimates hydraulic conductivities by roughly an order of magnitude.

Estimates for the more conductive blocks tend to show closer agreement. Possibly this is because the **K** tensors of such blocks tend to be dominated by large fractures that transect the entire block, and thus are less affected by irregular connectivity and tortuosity of flow paths composed of the smaller fractures.

A few blocks on the 100 m scale (about 10% of the total) yield permeameter estimates of hydraulic conductivity that are higher than the corresponding geometric estimates. For half of these blocks, the discrepancy is less than half an order of magnitude and may be explained by the way that directional conductivities have been averaged as $(K_x+K_y+K_z)/3$ for these plots. For the remaining cases (about 5% of all blocks for which permeameter flows were simulated), this result might be due to anomalous connections within the fracture network, or alternatively could be an artefact of cross-corner flows. The latter is an effect of the artificial boundary conditions for the permeameter simulations.

In terms of anisotropy of hydraulic conductivity (Figure 3.12), results from permeameter simulations are strikingly different from the geometrical estimates. Horizontal components (K_x and K_y) are dominant relative to the vertical component K_z, as for the geometrical estimates (and in contrast to the analytical estimates given in Table 3.2), but the ratio of K_x to K_y varies over a wide range. Several blocks are primarily conductive in just one horizontal direction (more often K_x than K_y). One block, which plots as an isolated point at the apex of the triangular plot, is conductive in the vertical direction but effectively non-conductive in the *x* and *y* directions.

Permeameter estimates of hydraulic conductivity for two different block scales, 50 m and 100 m for a single realization (Figure 3.13) agree within an order of magnitude or less for the more conductive blocks . Slightly more divergence is seen between scales for the lower-conductivity blocks. Overall the effect of block scale appears to be minor to moderate, for blocks in this range of block sizes.

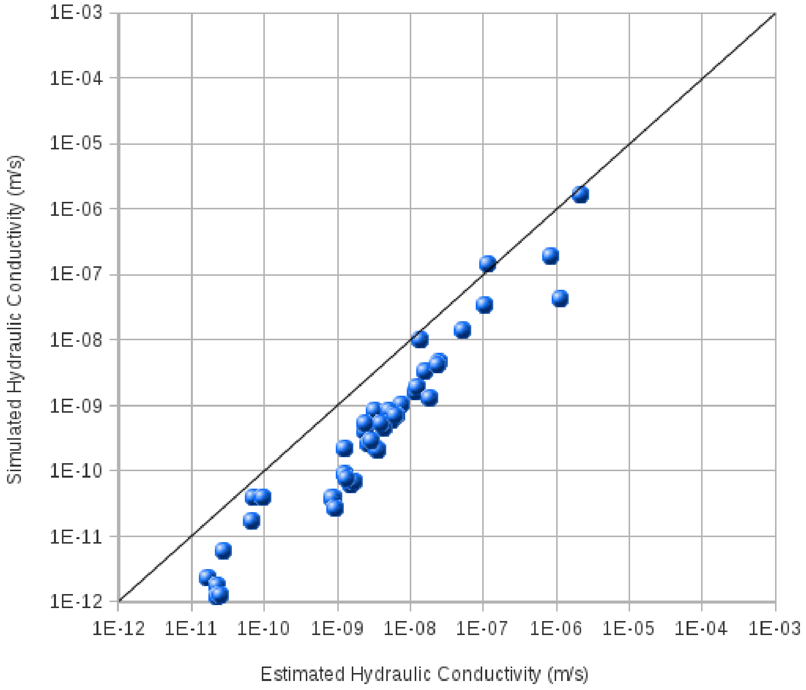

Figure 3.10 Comparison of permeameter estimates of DFN hydraulic conductivity versus geometrical estimates, for a single realization of the 50 m block scale. Hydraulic conductivity is plotted as the mean of the directional conductivities (K_x+K_y+K_z)/3.

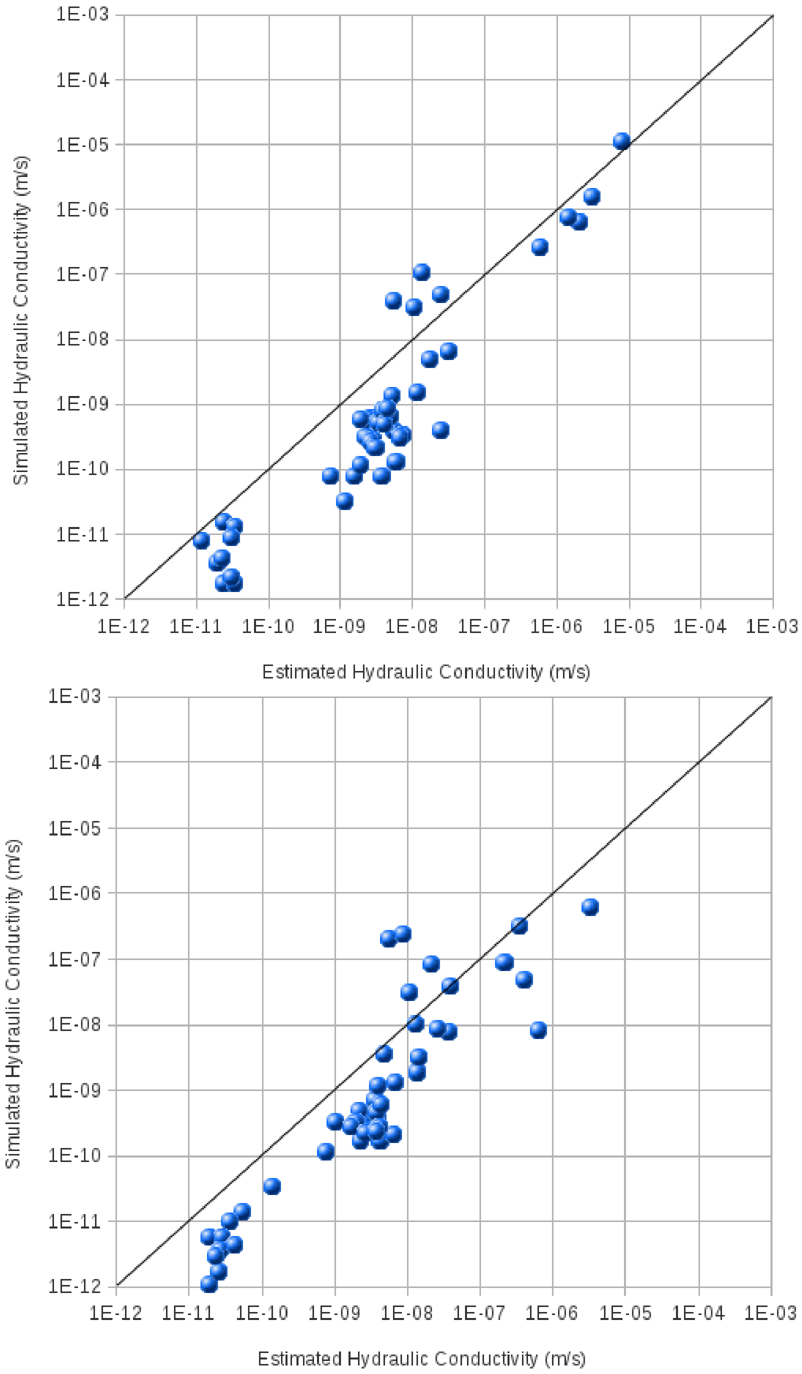

Figure 3.11 Comparison of permeameter estimates of DFN hydraulic conductivity versus geometrical estimates, for two realizations of the 100 m block scale. Hydraulic conductivity is plotted as the mean of the directional conductivities (K_x+K_y+K_z)/3.

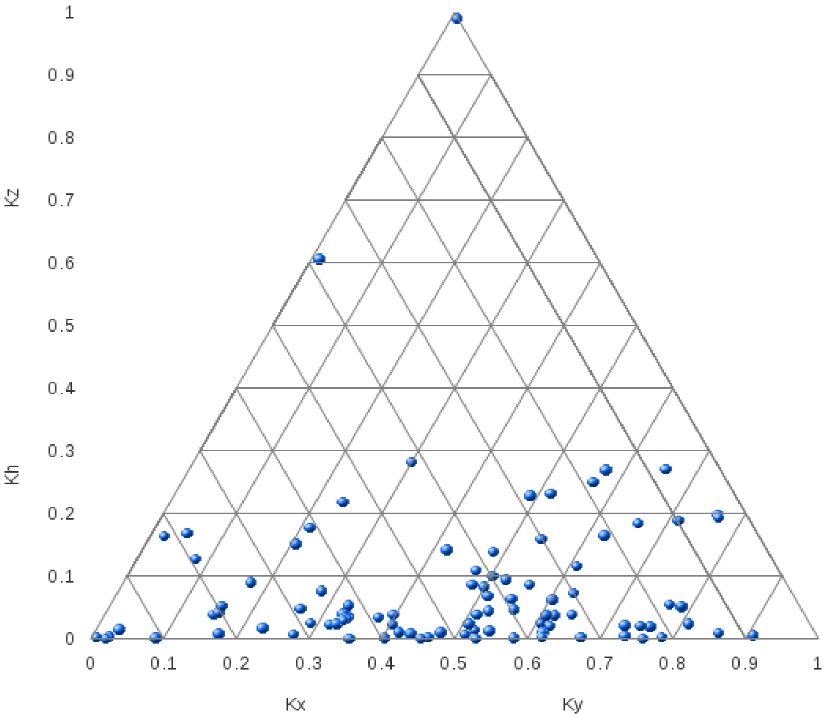

Figure 3.12 Anisotropy ratios for block-scale hydraulic conductivity tensors estimated by permeameter simulations from DFN simulations for 94 blocks, all depths. The horizontal grid lines represent equal ratios of vertical vs. horizontal conductivity. The grid lines that slope downward toward the right represent equal ratios of K_x versus conductivity in the *Y-Z* plane. The grid lines that slope upward toward the right represent equal ratios of K_y versus conductivity in the *X-Z* plane. Points near the corners of the triangular plot represent blocks for which the effective hydraulic conductivity is close to unidirectional.

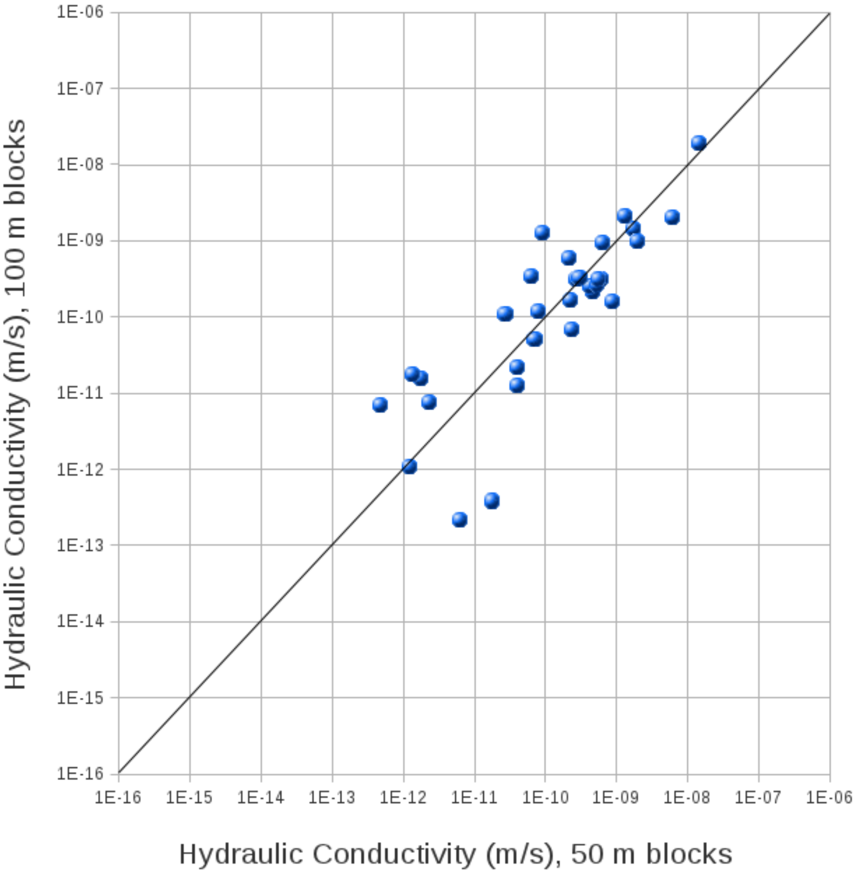

Figure 3.13. Comparison of geometrical estimates of hydraulic conductivity for 50 m and 100 m block scales. Results are for the same realization and sampling of grid cells as in Figure 3.1.

The permeameter simulations also produced flux-weighted estimates of porosity and flow-wetted surface. These flux-weighted estimates are likely to be more representative of the preferential flow paths through a given rock block, than the geometric estimates presented in the preceding section.

Figure 3.14 compares flux-weighted estimates of these two quantities, based on the weighting formulae defined in Section 2.2.3. The "q-weighted" estimates $<\theta>_q$ and $<a_r>_q$ are weighted with respect to the flux in each element, and thus emphasize the elements that carry the highest groundwater flux. The "qA-weighted" estimates $<\theta>_{qA}$ and $<a_r>_{qA}$ are weighted with respect to the product of flux times element area, to dilute the impact of a few small elements that may have high fluxes (in some cases possibly affected by locally poor precision in the numerical solution, particularly narrow elements with high aspect ratios).

Both types of flux-weighted estimates are lower than the geometrical estimates by 3 to 4 orders of magnitude. The q-weighted averages $<\theta>_q$ and $<a_r>_q$ are both roughly 4 orders of magnitude lower than the corresponding the geometrical estimates of θ and a_r. The qA-weighted averages $<\theta>_{qA}$ and $<a_r>_{qA}$ are both roughly 3 orders of magnitude lower than the corresponding the geometrical estimates of θ and a_r. These large differences indicate that the main flow paths through the DFN networks, on the 100 m block scale, access only a small fraction (0.1% to 0.01%) of the total area of the transmissive fractures. This is understandable considering that the geometrical calculations include all transmissive fractures, not just hydraulically connected fractures, while the flux-weighted estimates emphasize the hydraulically connected fractures.

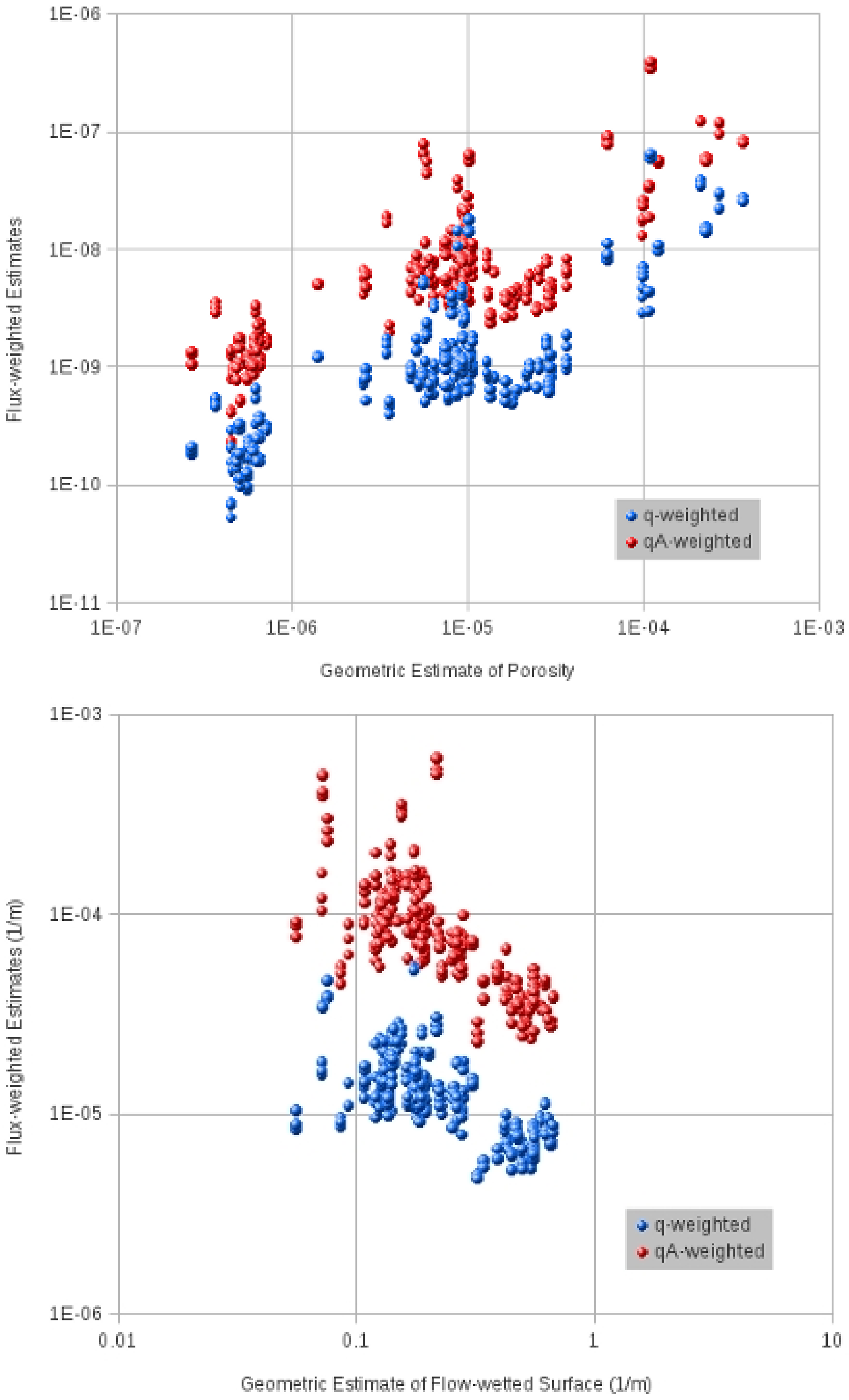

Figure 3.14. Comparison of geometrical estimates and flux-weighted estimates for (a) porosity and (b) flow-wetted surface, both for the 100 m block scale.

3.2. Interaction of natural fractures with EDZ

3.2.1. Effect of EDZ on block-scale hydraulic conductivity

Block-scale flow and transport was simulated for a sample of six 100 m blocks at approximate repository depth (centered at $Z = -450$ m), in which an EDZ was included for a 100 m section of repository tunnel with deposition holes, by the conditional simulation methods described in Section 2.3. For these simulations, the sides of the blocks were aligned with the axes of the deposition tunnels in the proposed repository layout at Forsmark, nominally in the SE-NW direction.

For each block, four sets of permeameter simulations were performed to test different degrees of EDZ continuity. These runs considered EDZ continuity factors c_{EDZ} ranging from $c_{EDZ} = 0$ (no significant EDZ) to $c_{EDZ} = 1$ (continuous EDZ), with intermediate factors of $c_{EDZ} = 0.5$ and $c_{EDZ} = 0.75$.

Effective hydraulic conductivities for flow in response to a head gradient parallel to the axis of the tunnel (decreasing from SE to NW) in these blocks are shown as a function of EDZ continuity in Figure 3.15. For the cases with $c_{EDZ} \geq 0.5$, the block-scale conductivities are all very similar. However, a decrease is seen for K parallel to the tunnel axis, for the case where the EDZ is suppressed ($c_{EDZ} = 0$). For flow in the other two orthogonal directions (SW to NE and vertical), results for all values of c_{EDZ} are practically identical.

The transmissivity of the EDZ is $1\text{x}10^{-8}$ m^2/s (per SKB's design specification). The circumference of the EDZ feature in cross-section is 2((4.2 m + 2 m) + (4.8 m + 2 m)) = 26 m. Thus the contribution to hydraulic conductivity in the axial direction due to the EDZ, for a 100 m cube, is:

$$(\ 26\text{ m })(\ 1\text{x}10^{-8}\text{ m}^2/\text{s})/(100\text{m x }100\text{ m}) = 2.6\text{x}10^{-11}\text{ m/s}$$

Thus the axial conductivity due to a continuous EDZ along the tunnel, with this level of transmissivity, could be significant compared to the effective hydraulic conductivity of some low-*K* rock blocks at repository depth. Indeed two of the blocks in Figure 3.15 show hydraulic conductivities close to this value, when an EDZ is present.

However, the axial *K* values of the other blocks are higher than the EDZ could account for directly. In these cases, apparently the EDZ serves to form connections between fractures that are more transmissive than the EDZ itself. The EDZ apparently can play this role of enhancing connections in the DFN, even when it is 50% discontinuous ($c_{EDZ} = 0.5$).

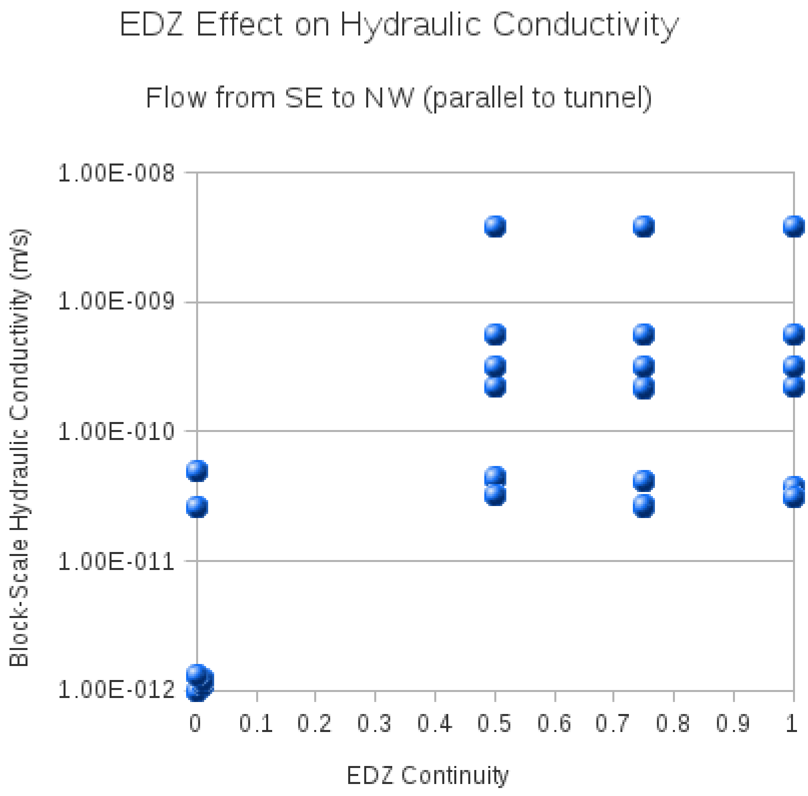

Figure 3.15 Effective directional hydraulic conductivity in the SE-NW direction for simulated 100 m blocks at repository depth (Z = -450 m) containing a 100 m section of deposition tunnel oriented in the same direction, for different degrees of continuity of the excavation damage zone (EDZ). A value of 0 on the horizontal axis corresponds to the case where the entire EDZ has been reduced to a negligible value of transmissivity ($T_{EDZ} = 10^{-13}$ m^2/s). A value of 1 corresponds to the case where a continuous EDZ with $T_{EDZ} = 10^{-8}$ m^2/s. Intermediate values c represent cases where a corresponding fraction (1-c) of the finite elements belonging to the EDZ have randomly been set to have a negligible transmissivity, so just the fraction c have $T_{EDZ} = 10^{-8}$ m^2/s.

3.2.2. Ranges of groundwater flux to deposition holes

Groundwater fluxes to deposition holes were calculated for each of the block-scale flow simulations. The results are plotted in Figure 3.16 as cumulative distributions for each of the directions for the imposed hydraulic gradient: SE-NW (parallel to the tunnel axis), SW-NW (perpendicular to the tunnel axis), and vertically upward.

Note that these distributions are for an imposed head gradient of 0.001 m per m. This is an arbitrarily chosen but reasonable value for the block-scale simulations. A simple evaluation of the potential for groundwater flow at the Forsmark site (Geier, 2012) based on topographic gradients yielded upper-bound estimates in the range 0.00125 to 0.005. The flow to deposition holes calculated from this type of model (saturated flow and linearly varying specified-head boundary conditions) scales linearly with the magnitude of the applied head gradient.

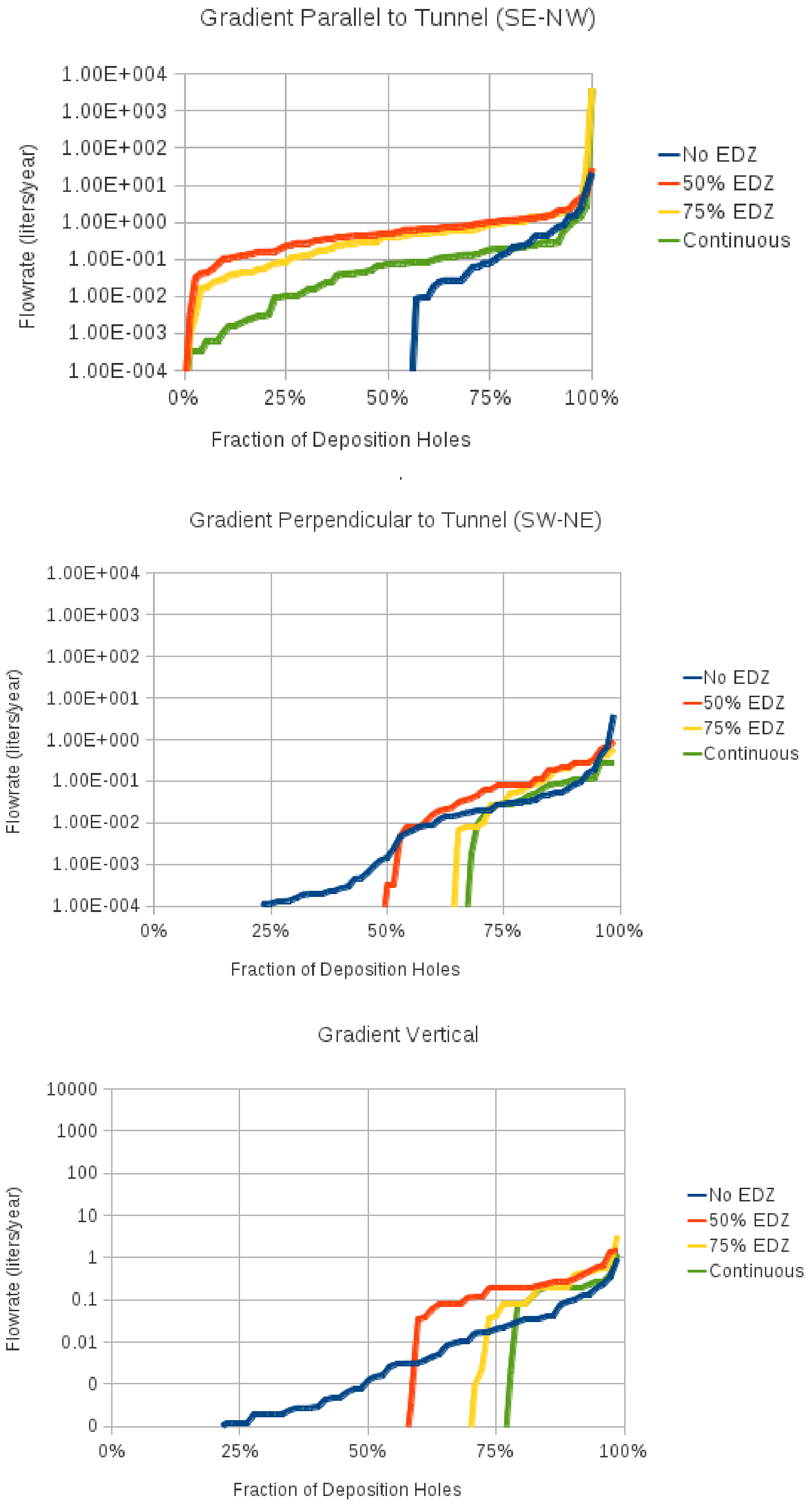

Figure 3.16 Distribution of flowrates to deposition holes in the block-scale EDZ simulations, in response to a head gradient of 0.001 imposed (a) parallel to the tunnel axis, (b) perpendicular to the tunnel axis, and (c) vertical.

For a SE-NW head gradient (parallel to the axis of the deposition tunnel), in the case of negligible EDZ transmissivity (“No EDZ” in the plots), fewer than half of the deposition holes experience a flowrate of more than 0.1 milliliters/year (mL/y). However nearly all of these yield at least 10 mL/y (possibly a more realistic threshold value for numerical resolution), and about 10% of the holes yield 1 L/y or more.

The presence of a continuous EDZ with transmissivity of 10^{-8} m^2/s increases the number of deposition holes with at least small calculated flows. Since all deposition holes are intersected by the EDZ in the floor of the tunnel, 100% of the holes are calculated to receive at least 0.1 mL/y. However, the fractions receiving more than 0.1 L/y and more than 1 L/y are essentially the same as for the “No EDZ” case, considering the small sample size.

For an EDZ with reduced continuity, the flowrates in the lower end of the distribution are increased. The fractions receiving more than 0.1 L/y and more than 1 L/y increase with decreasing EDZ continuity, at least in the range $c_{EDZ} > 0.5$.

A possible interpretation of this surprising result is that, for $1 > c_{EDZ} > 0.5$, there are still enough transmissive elements in the EDZ that a conductive path will generally exist along the perimeter of the tunnel. The effect of reducing c_{EDZ} in this range may be to focus flows through a smaller portion of the EDZ (and connected DFN fractures), resulting in increased flows in the lower end of the distribution. However, for the deposition holes with the highest flows, which are determined by higher-transmissivity fractures, the flow distribution is less sensitive to EDZ continuity.

For a SW-NE head gradient (perpendicular to the axis of the deposition tunnel), both the “No EDZ” and $c_{EDZ} = 0.5$ cases yield a similar fraction of deposition holes with flows of at least 10 mL/y. The $c_{EDZ} = 0.75$ and continuous-EDZ cases yield progressively higher fractions of deposition holes with flows of 10 mL/y or more.

The cases with $c_{EDZ} = 0.75$and $c_{EDZ} = 0.5$ both yield higher fractions of deposition holes with flows of 0.1 L/y or more. However, considering the small number of deposition holes in the sample (six blocks with 12 deposition holes per block, so 72 deposition holes total), the differences in the upper parts of the flow distribution are minor.

Results for a vertical head gradient are qualitatively similar to those for a SW-NE head gradient. In both cases, presumably the EDZ plays a secondary role in determining the magnitudes of flows, which must find their way through the block via paths that are composed at least partly of stochastic fractures. Neither of these cases produces flows in excess of 10 L/y, which are predicted to occur for at least a few percent of deposition holes for cases in which the imposed head gradient is parallel to the tunnel.

3.2.3. Particle-tracking trajectories

Particle-tracking to simulate advective-dispersive transport from deposition holes yields results in terms of trajectories for individual particles. Visualizations of these trajectories can be informative for understanding the patterns of flow which features control transport from the source locations.

Figures 3.17 through 3.19 show the time-dependent particle trajectories that were obtained for each of the three orientations of head gradient, six sampled blocks, and four different levels of EDZ continuity. All of the trajectories are shown in plan view. The plots are organized eight per page, with the four upper plots representing the first sampled block, and the four lower plots representing the second sampled block. For each block and flow direction, the arrangement of the four plots is the same: (i) continuous EDZ (upper left), (ii) 75% EDZ (upper right), (iii) 50% EDZ (lower left), and (iv) no EDZ.

The colors of particle-trajectory segments in these figures indicate the age of particles as they pass along those segments. Particles may exit the boundaries in the direction perpendicular to the cross section. Or, in some cases they may become stuck in portions of the computational mesh with very low gradients or poorly conditioned mesh geometries. In such cases the color of the trajectory in the plot shows the age of the particle up to the point when it reached the stagnant or problematic-geometry part of the mesh.

For the case of a SE-NW head gradient parallel to the tunnel axis, the continuous-EDZ cases (upper-left-hand in each group of four plots) show a mostly coherent pattern, dominated by trajectories that mostly follow the EDZ along the tunnel. The simplest patterns (Cases 010 and 023) indicate flow directly along the tunnel EDZ. Cases 039 and 044 (Figure 3.17e,f) yield slightly more complicated patterns in which particles veer to the north as they travel along the EDZ, due to the influence of intersecting fractures. Still more complicated patterns are produced in Cases 021 and 038 where some particles even make excursions into the DFN around the EDZ.

Reduction in EDZ continuity to the $c_{EDZ} = 0.75$ and $c_{EDZ} = 0.5$ levels leads to progressively more complicated patterns as the particles are forced to seek out more tortuous paths through the EDZ. For the case of $c_{EDZ} = 0.5$, increasing numbers of particles do not reach the outflowing boundary by the time limit of 10^8 s.

For the “No EDZ” case where all EDZ elements have been set to a very low value of transmissivity (10^{-13} m^2/s), the particle trajectories become more regular. However, particle ages in these plots are dominated by younger particles (blue and green colors). These particles may travel appreciable distances due to the assumed square-root correlation of transport aperture to transmissivity. However most eventually terminate due to irregular numerical gradients which are encountered at these very low levels of flow.

For head gradients in the other directions (SW-NE or upward), particle trajectories (Figures 3.18 and 3.19, respectively are much more irregular and apparently much more strongly influenced by the irregularities of the surrounding discrete-fracture network. In a few cases, it can be seen that the particles make use of the EDZ (including in the “No EDZ” case where transmissivity is small but non-zero, and the EDZ apertures that control transport velocities are correspondingly small).

Detailed inspection of the particle trajectories shows that a high proportion of the particles released from a given deposition hole arrive at the next deposition hole downstream, particularly for the case of flow aligned with the tunnel axis. This type of transport behavior has previously been noted in site-scale models of a repository at the Forsmark site (Geier, 2010)..

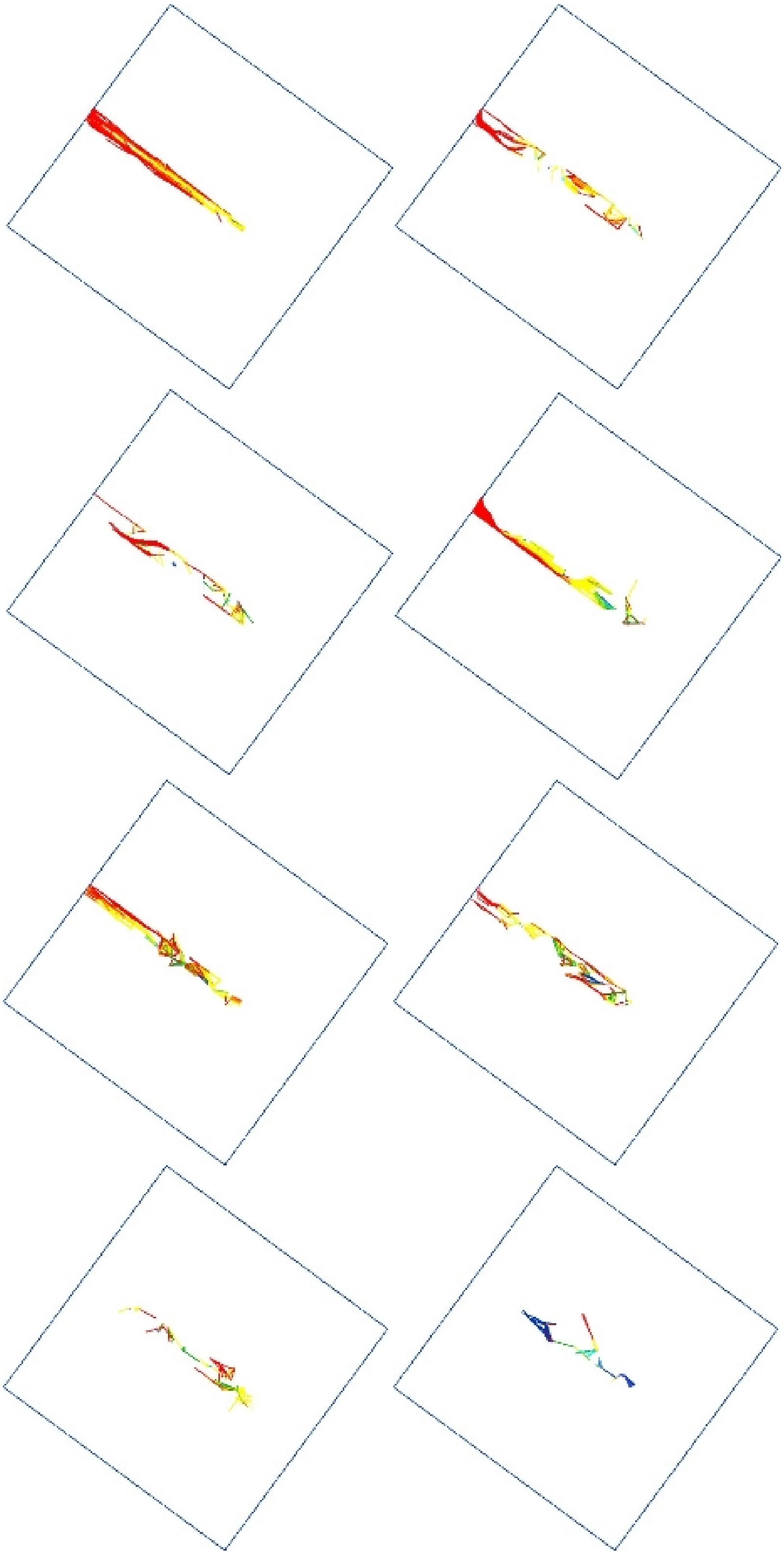

Figure 3.17a,b Particle trajectories for SE-NW flow in response to a hydraulic gradient parallel to the deposition tunnel. Results for two block-scale realizations (010 and 021), and four cases for each (continuous EDZ, 75% EDZ, 50% EDZ, and no EDZ). Colors of the particle trajectories are representative of particle age for each segment of the trajectory, ranging from blue for younger particles through red for particles that reach the maximum age of 10^8 s (3.17 years).

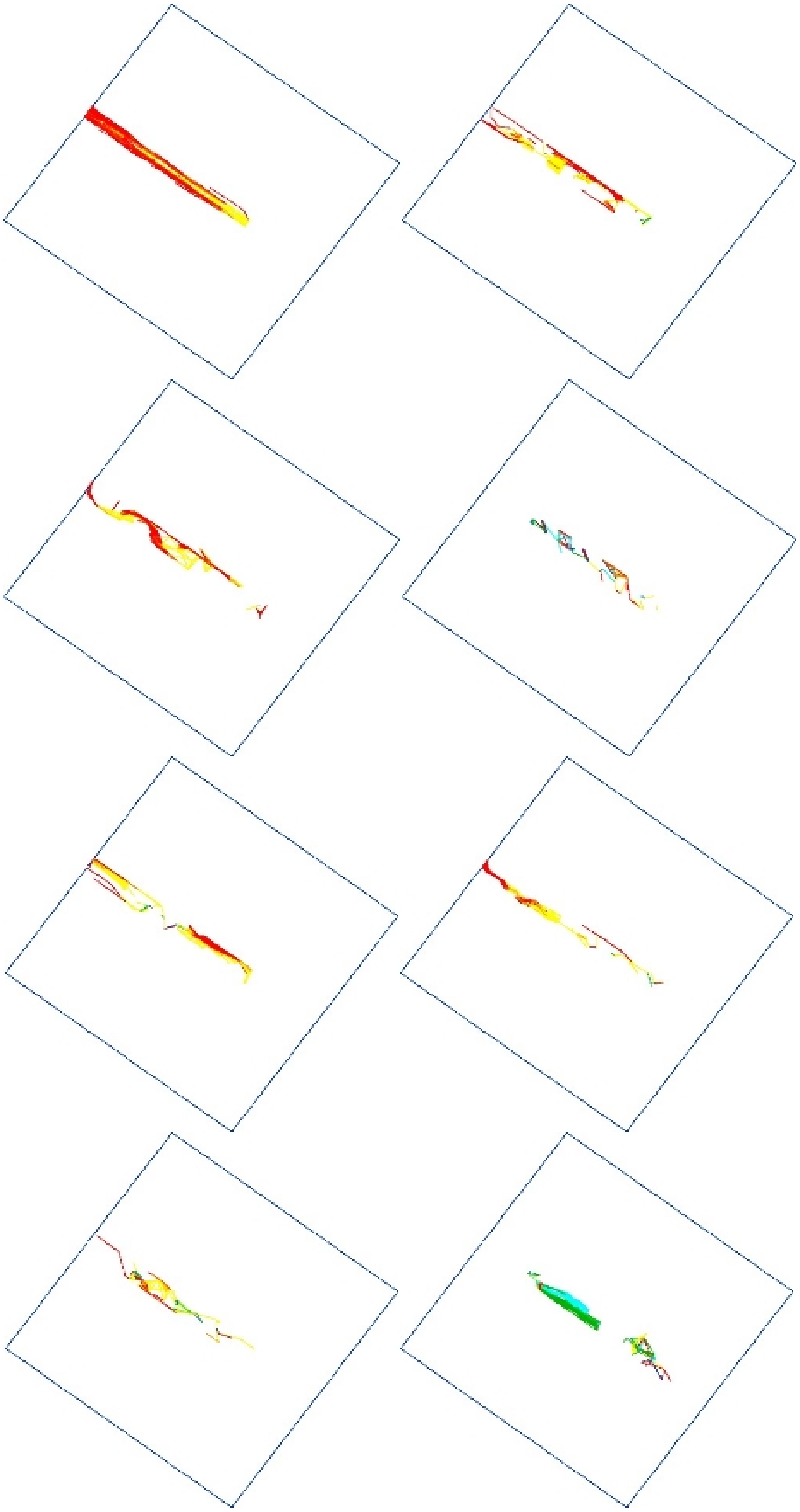

Figure 3.17c,d Particle trajectories for SE-NW flow in response to a hydraulic gradient parallel to the deposition tunnel. Results for two block-scale realizations (023 and 038), and four cases for each (continuous EDZ, 75% EDZ, 50% EDZ, and no EDZ). Colors of the particle trajectories are representative of particle age for each segment of the trajectory, ranging from blue for younger particles through red for particles that reach the maximum age of 10^8 s (3.17 years).

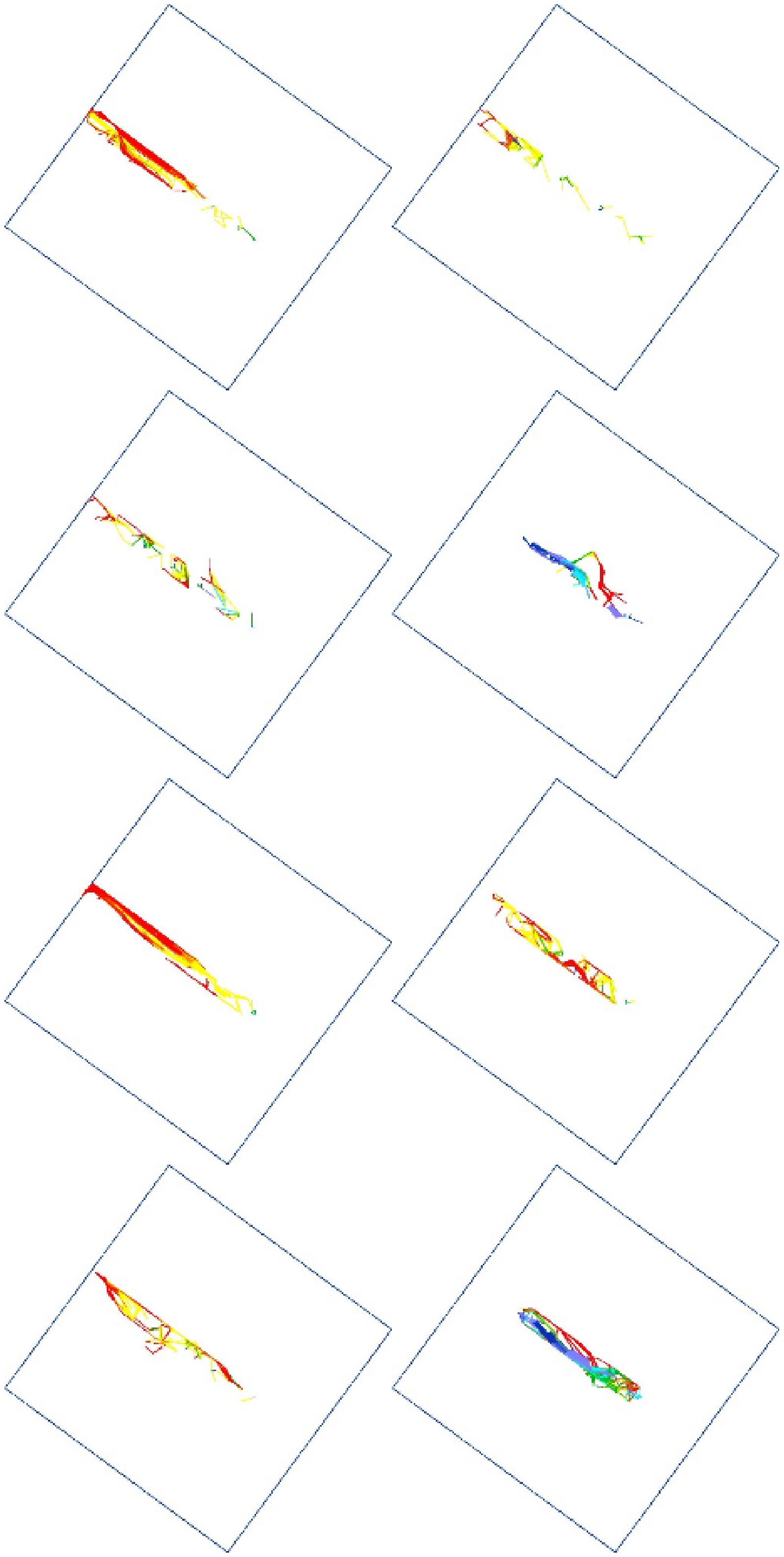

Figure 3.17e,f Particle trajectories for SE-NW flow in response to a hydraulic gradient parallel to the deposition tunnel. Results for two block-scale realizations (039 and 044), and four cases for each (continuous EDZ, 75% EDZ, 50% EDZ, and no EDZ). Colors of the particle trajectories are representative of particle age for each segment of the trajectory, ranging from blue for younger particles through red for particles that reach the maximum age of 10^8 s (3.17 years).

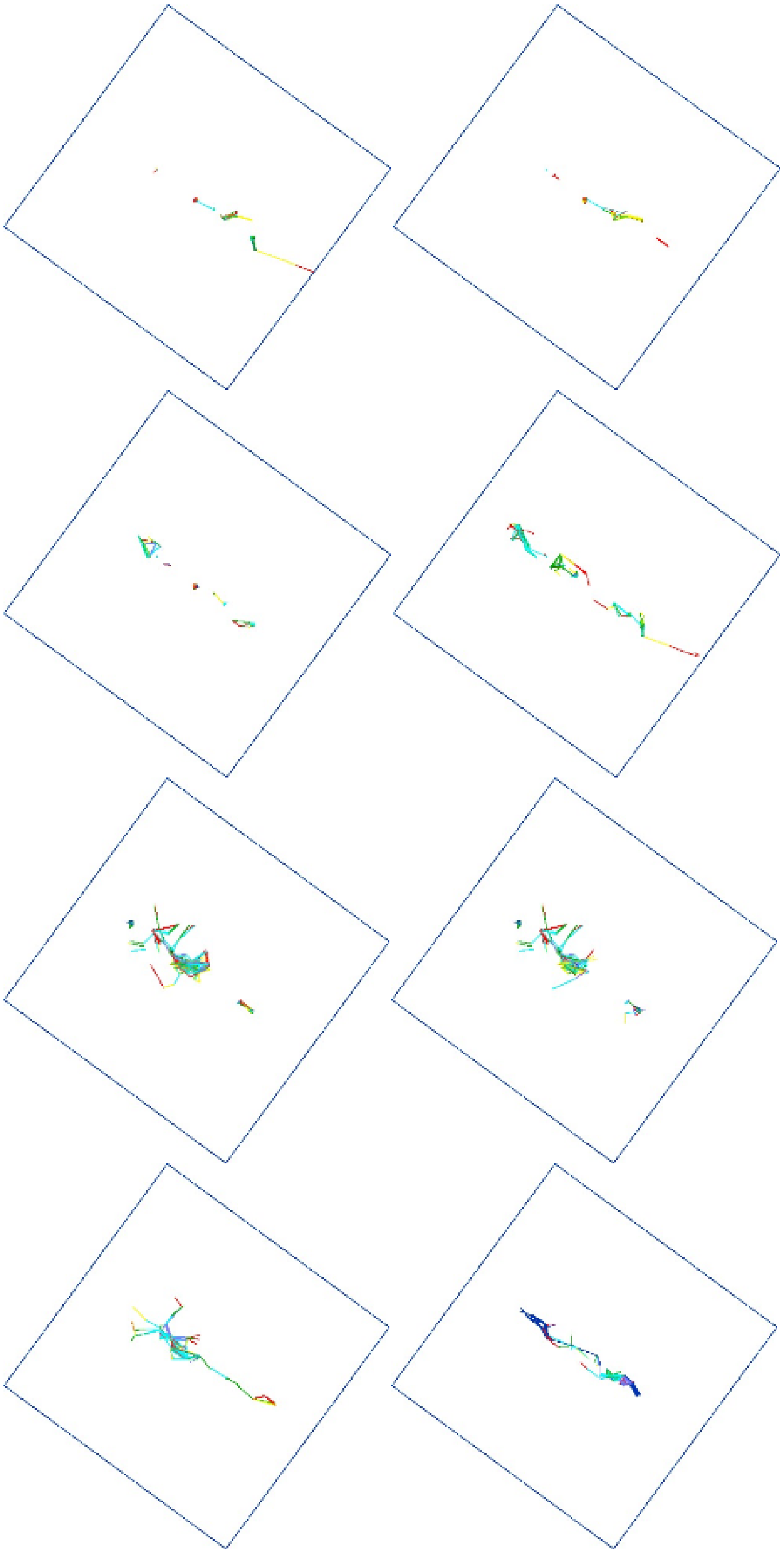

Figure 3.18a,b Particle trajectories for SW-NE flow in response to a hydraulic gradient perpendicular to the deposition tunnel. Results for two block-scale realizations (010 and 021), and four cases for each (continuous EDZ, 75% EDZ, 50% EDZ, and no EDZ). Colors of the particle trajectories are representative of particle age for each segment of the trajectory, ranging from blue for younger particles through red for particles that reach the maximum age of 10^8 s.

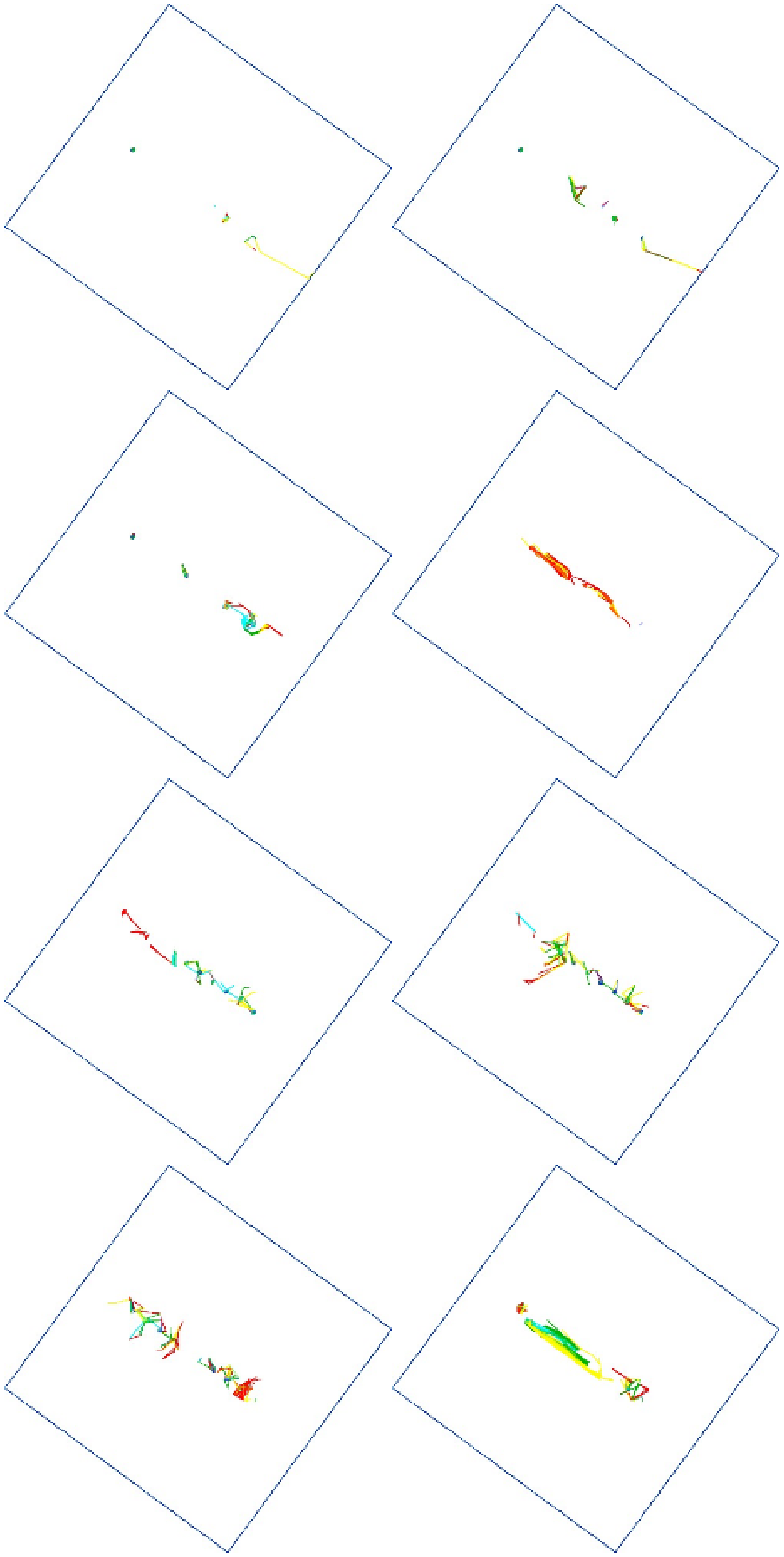

Figure 3.18c,d Particle trajectories for SW-NE flow in response to a hydraulic gradient perpendicular to the deposition tunnel. Results for two block-scale realizations (023 and 038), and four cases for each (continuous EDZ, 75% EDZ, 50% EDZ, and no EDZ). Colors of the particle trajectories are representative of particle age for each segment of the trajectory, ranging from blue for younger particles through red for particles that reach the maximum age of 10^8 s.

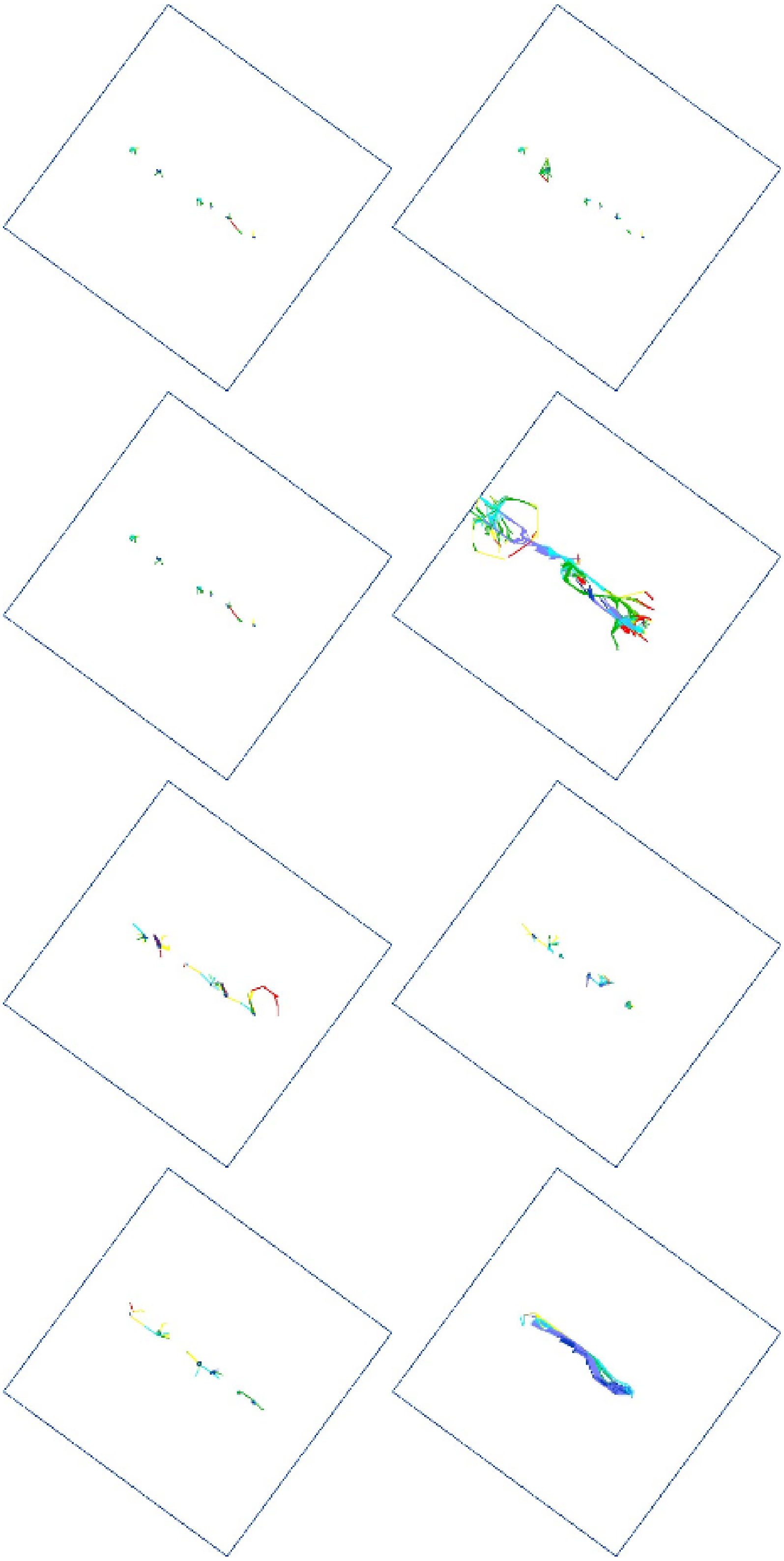

Figure 3.18e,f Particle trajectories for SW-NE flow in response to a hydraulic gradient perpendicular to the deposition tunnel. Results for two block-scale realizations (039 and 044), and four cases for each (continuous EDZ, 75% EDZ, 50% EDZ, and no EDZ). Colors of the particle trajectories are representative of particle age for each segment of the trajectory, ranging from blue for younger particles through red for particles that reach the maximum age of 10^8 s.

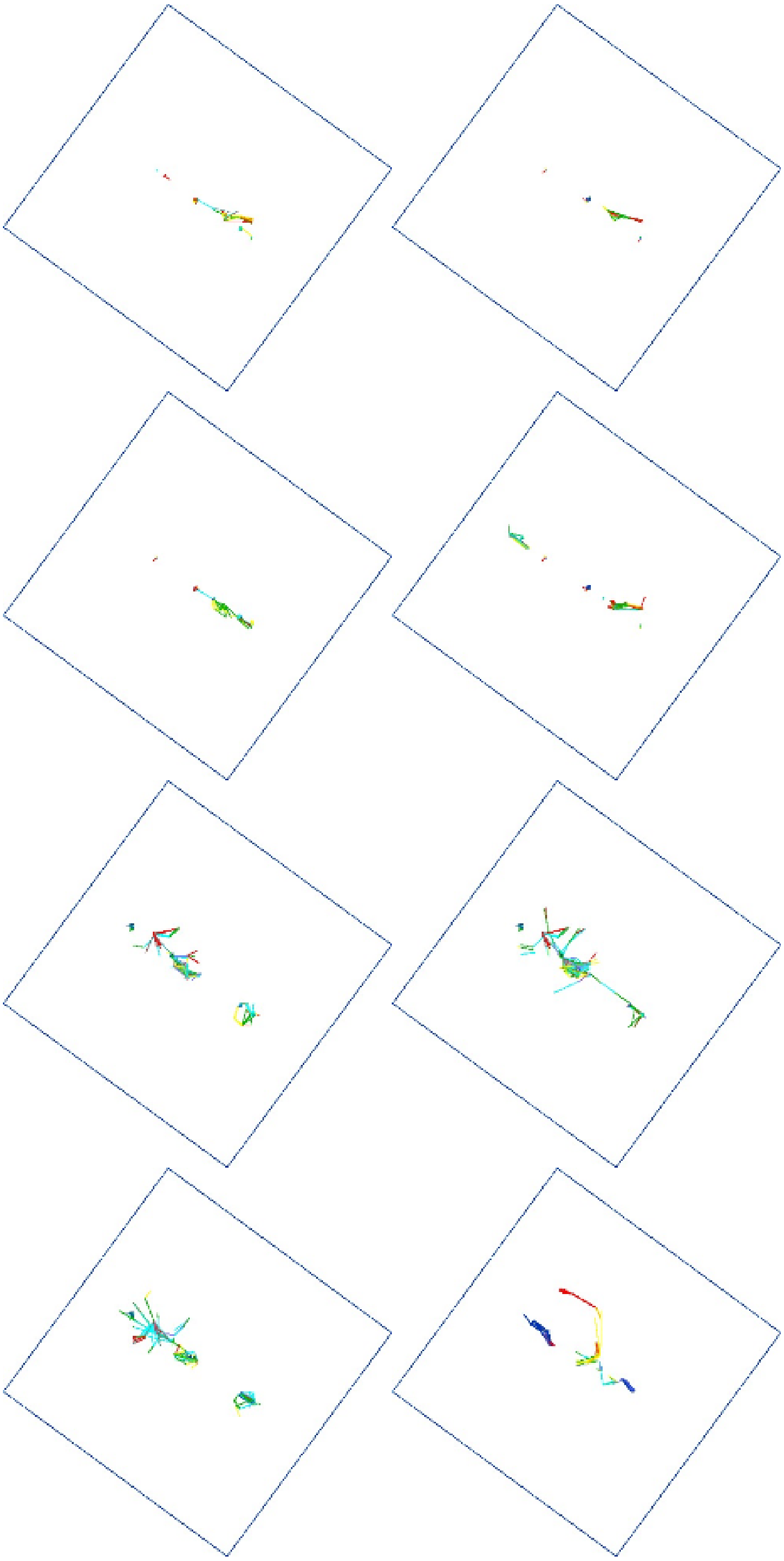

Figure 3.19a,b Particle trajectories for upward flow in response to a vertical hydraulic gradient. Results for two block-scale realizations (010 and 021), and four cases for each (continuous EDZ, 75% EDZ, 50% EDZ, and no EDZ). Colors of the particle trajectories are representative of particle age for each segment of the trajectory, ranging from blue for younger particles through red for particles that reach the maximum age of 10^8.

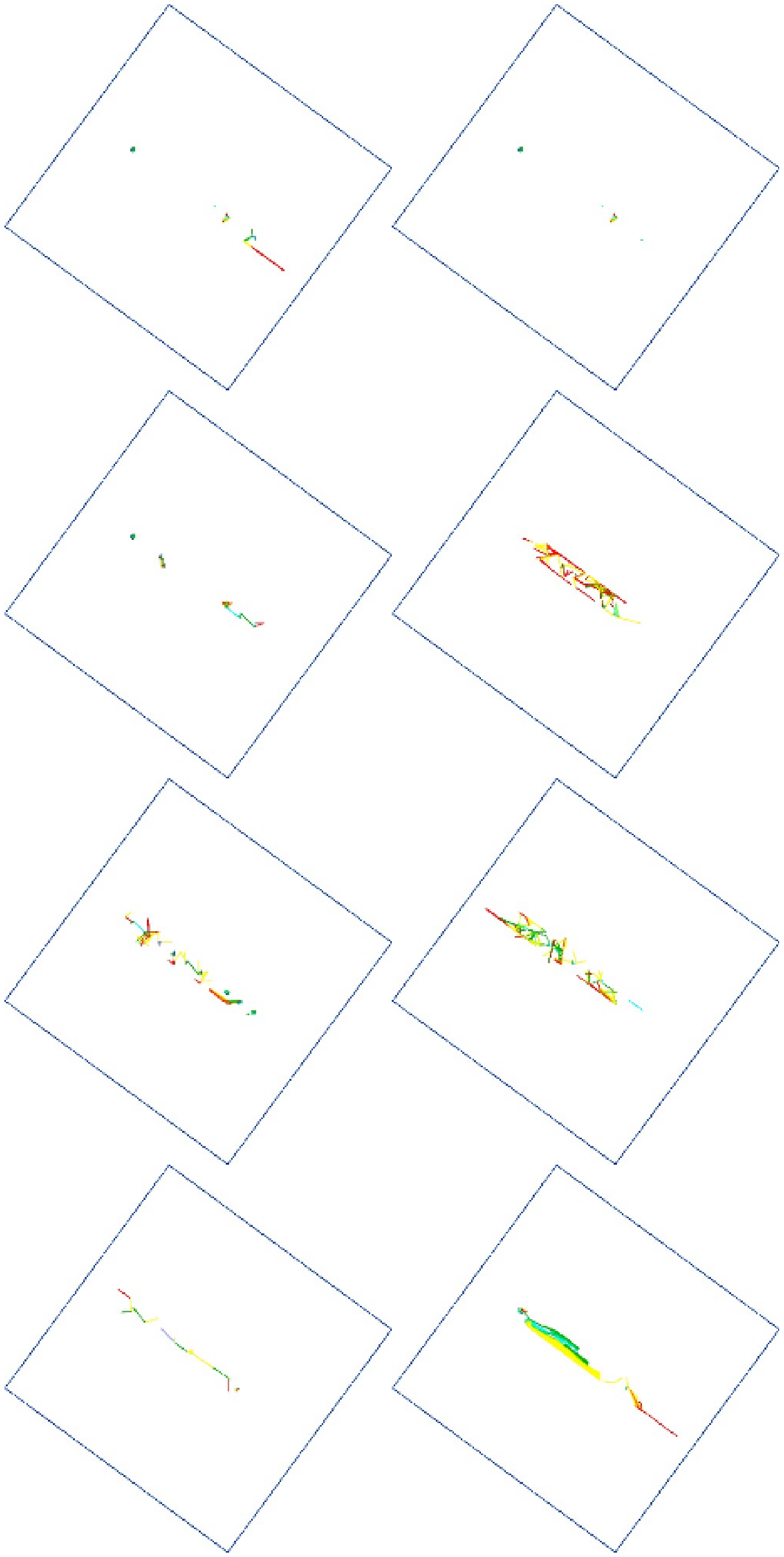

Figure 3.19c,d Particle trajectories for upward flow in response to a vertical hydraulic gradient. Results for two block-scale realizations (023 and 038), and four cases for each (continuous EDZ, 75% EDZ, 50% EDZ, and no EDZ). Colors of the particle trajectories are representative of particle age for each segment of the trajectory, ranging from blue for younger particles through red for particles that reach the maximum age of 10^8.

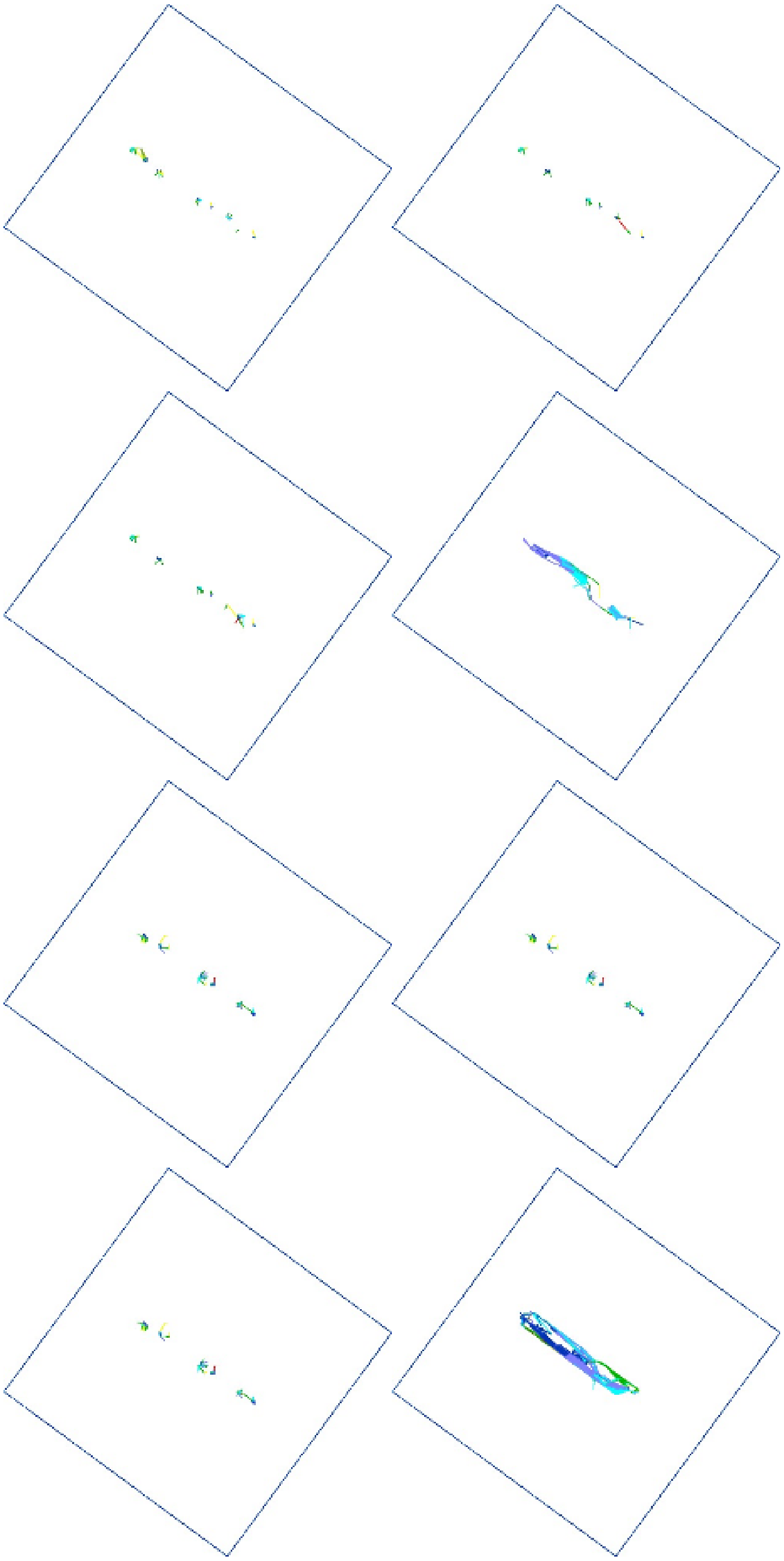

Figure 3.19e,f Particle trajectories for upward flow in response to a vertical hydraulic gradient. Results for two block-scale realizations (039 and 044), and four cases for each (continuous EDZ, 75% EDZ, 50% EDZ, and no EDZ). Colors of the particle trajectories are representative of particle age for each segment of the trajectory, ranging from blue for younger particles through red for particles that reach the maximum age of 10^8.

3.2.4. Transport resistance

Estimates of transport resistance (*F*) as a function of transport distance, for flow and transport simulations in response to head gradients in the three orthogonal directions, are presented in Figures 3.20 through 3.22.

A general feature of these plots is that, regardless of the direction of the head gradient, for short transport distances ($L < 10$ m) the points are clustered along at least two distinct lines of 1:1 slope that represent approximately linear increases of F with transport distance. These apparently represent transport paths that are dominated by different classes of features (EDZ versus discrete fractures). In some cases there are additional lines of 1:1 slope that represent fractures with distinctly different ratios of transmissivity to aperture (and hence transmissivity to wetted surface).

At longer transport distances (10 m < L < 100 m) there is a tendency for these lines to blend into a cloud of points which is intermediate to the correlation lines for shorter transport distances. This is interpreted here as the range of scales over which the transport resistance *F* begins to represent the cumulative properties of multiple features (for example, a pathway that is partly via the EDZ and partly via DFN fractures).

However, the relationship between *L* and *F* is still evolving at the scale of $L = 100$ m, so further scale-dependence should be expected at larger scales of transport via tunnels in the DFN model that represents the rock mass.

The obtained distribution of *F* values for *L* approaching 100 m is however appropriate for scoping the consequences of transport through the rock mass and tunnel EDZ on a similar scale.

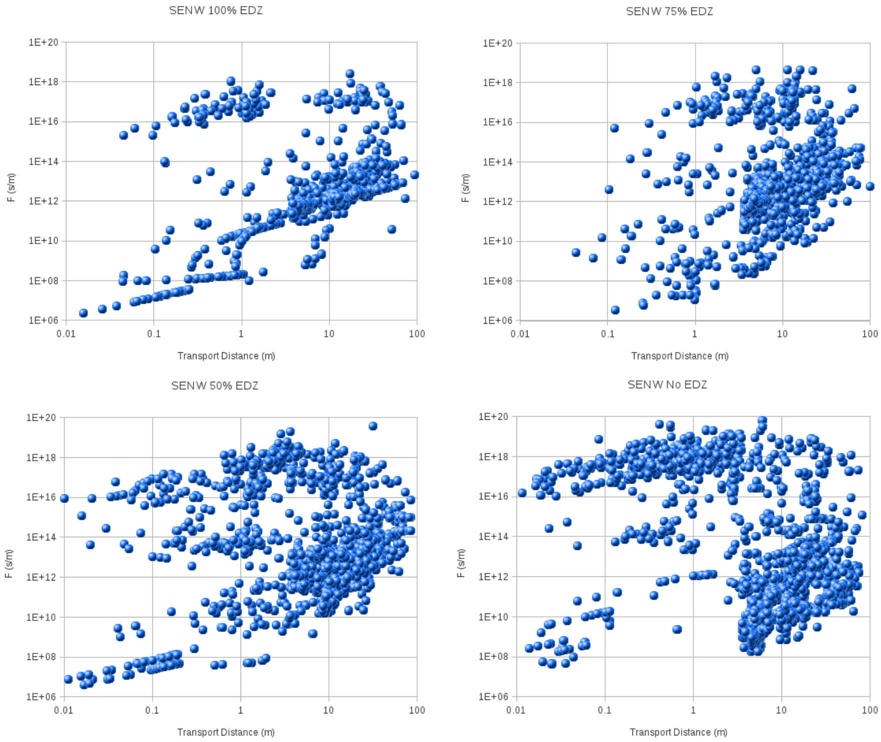

Figure 3.20 Transport resistance *F* as a function of transport distance from particles released from deposition holes in flow field produced by head gradient in SE-NW direction, parallel to tunnel axis. Results for cases of continuous EDZ, 75% EDZ, 50% EDZ, and no EDZ.

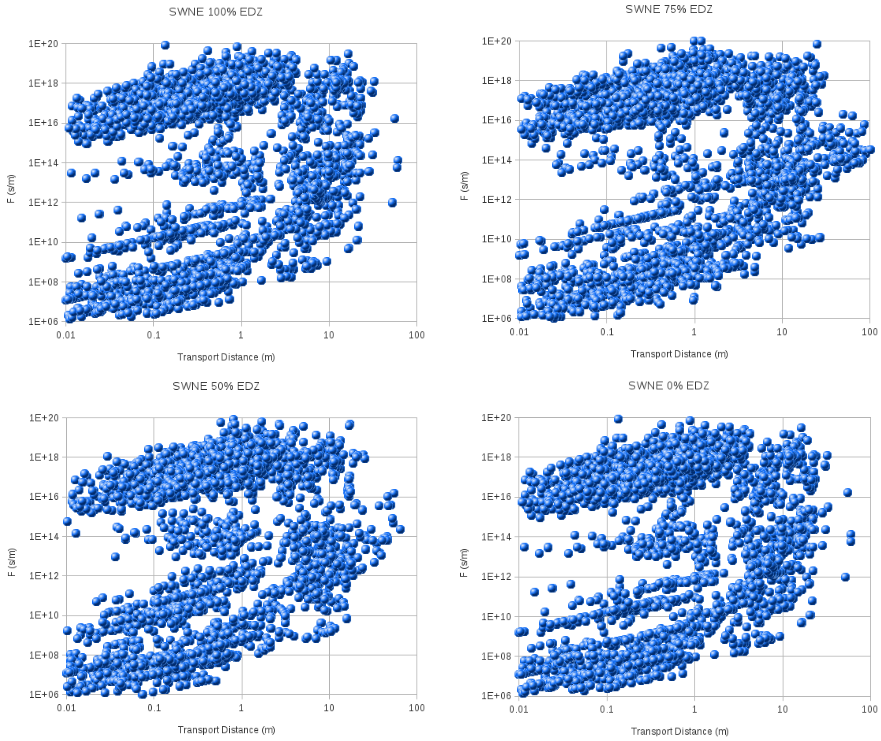

Figure 3.21 Transport resistance *F* as a function of transport distance from particles released from deposition holes in flow field produced by head gradient in SW-NE direction, perpendicular to tunnel axis. Results for cases of continuous EDZ, 75% EDZ, 50% EDZ, and no EDZ.

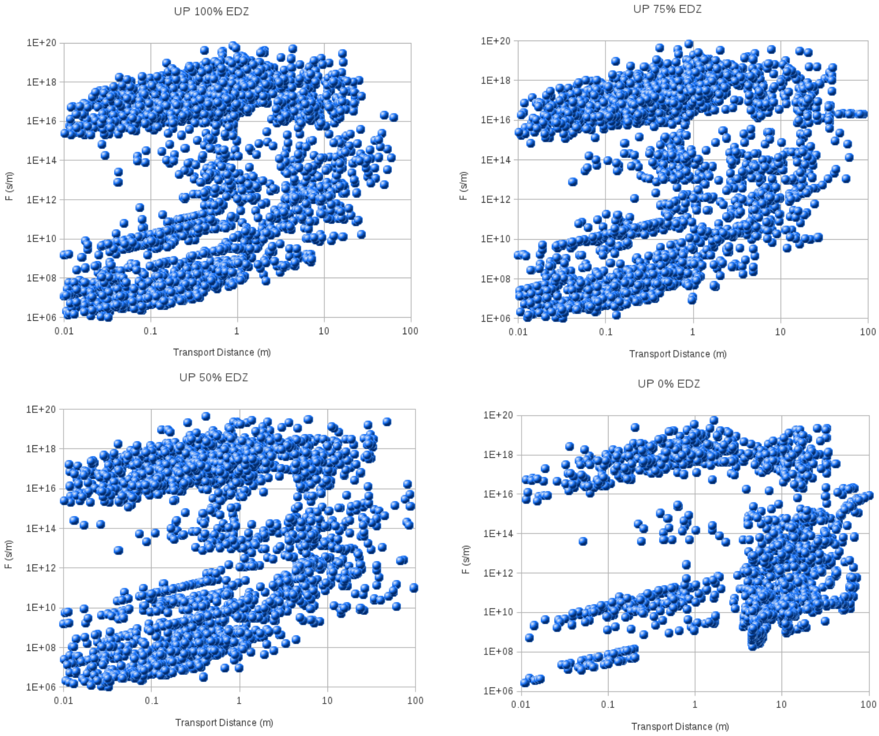

Figure 3.22 Transport resistance *F* as a function of transport distance from particles released from deposition holes in flow field produced by head gradient in upward (vertical) direction. Results for cases of continuous EDZ, 75% EDZ, 50% EDZ, and no EDZ.

3.3. Comparison with SKB results

Rock mass hydraulic properties including hydraulic conductivity **K**, porosity θ, and flow wetted surface a_r have been estimated by two different methodologies in the hydrogeological modeling for SR-Site. In models of the excavation and operational phases (Svensson and Follin, 2009) and of periods of periglacial and glacial conditions (Vidstrand et al., 2010), hydraulic conductivity in the hydraulic rock domains (HRDs) has been estimated by geometrical methods which are effectively the same as the methods described in Section 2.2.2 and applied in Section 3.1.2 of this report. In models of temperate periods (Joyce et al., 2009), permeameter calculations have been used (at least for calculations of hydraulic conductivity), similar to the methods described in Section 2.2.3 and applied in Section 3.1.3.

Hydraulic conductivities calculated by geometrical methods are presented by Svensson and Follin (2009) and Vidstrand et al. (2010) in terms of permeability k, (units of m^2), whereas Joyce et al. (2009) and the present report use hydraulic conductivity K (units of m/s). Hydraulic conductivity is related to permeability as:

$$K = \frac{\rho_w g}{\mu_w} k$$

where ρ_w is the density of water (on the order of 1000 kg/m^3 though increasing with salinity), g is gravitational acceleration (about 9.81 m/s^2), and μ_w is the dynamic viscosity of water (on the order of 0.001 Pa·s). Both ρ_w and μ_w vary as functions of water salinity, temperature, and pressure, but for groundwater conditions at Forsmark, this variation is slight in comparison with the orders-of-magnitude variation in permeability. Here the round approximation $\rho_w g/\mu_w \approx 10^7\ m^{-1}s^{-1}$ is used for simplicity of comparison between calculated K and k values.

SKB's presentation of K and k values is mainly graphical (*e.g.* Figures 4-3, 5-2 and 5-3 of Joyce et al., 2009, Figures 4-20 and 4-21 of Svensson and Follin, 2009, and Figures 5-12 and 5-13 of Vidstrand et al., 2010). Svensson and Follin (2009, Figure 4-25) show the distribution of calculated grid-cell permeabilities with a cumulative density function (c.d.f.) plot, but their plot includes grid cells from all depths and domains, as well as grid cells that are dominated by deterministic HCDs (which are not part of the rock mass as considered for block-scale calculations in the present study).

Geometrically calculated k values from repository depth, as presented graphically by Svensson and Follin (2009) and reproduced here in Figure 3.23, appear to be consistent with the geometric estimates of K values for the same depth, as presented in Section 3.1.2, at least in terms of order of magnitude. The bimodal distribution of K estimates, as apparent in Figure 3.5, is also consistent with these results.

Svensson and Follin (2009) present only the vertical component of permeability, and do not present anisotropy ratios. The present study indicates that geometrical estimates of permeability should yield higher horizontal than vertical permeability (Figure 3.9), and that this effect is even stronger when permeameter simulations are used (Figure 3.12). The permeameter method (as used by Joyce et al., 2009 and in Section 3.1.3 of this report) likely yields a more accurate assessment of anisotropy. This might explain, at least in part, why an increase in horizontal vs. vertical anisotropy factors for the HRD was found to improve the match of ECPM models to observations (Svensson and Follin (2009), p. 29; Vidstrand et al., 200 9, p. 45).

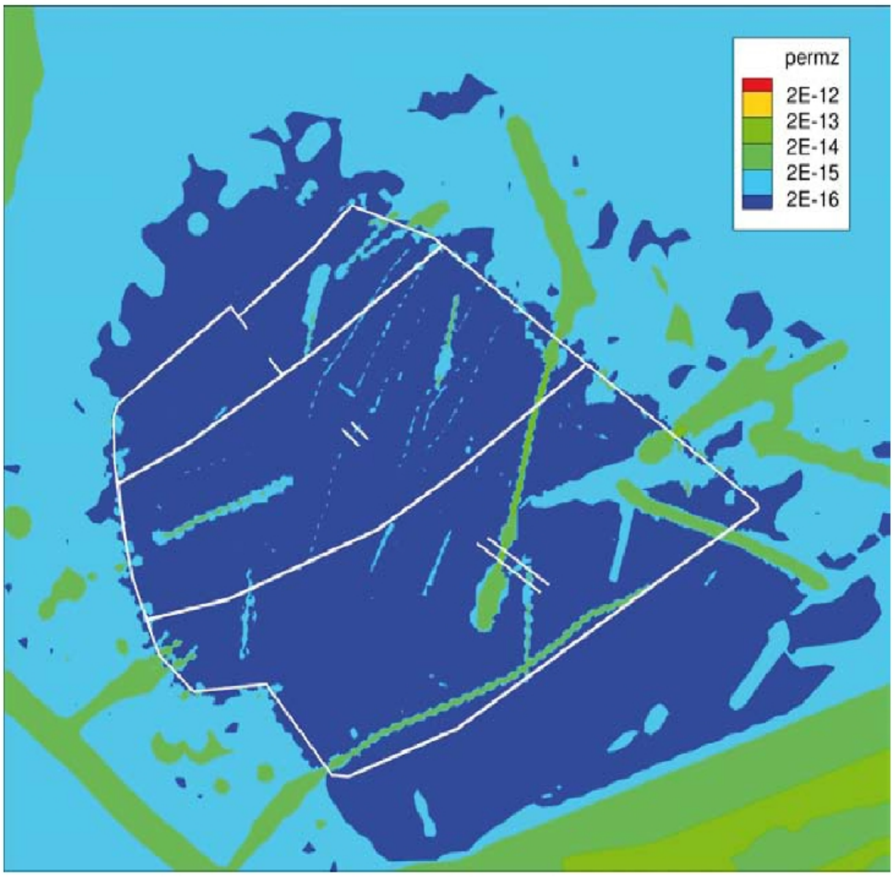

Figure 3.23 Calculated grid cell vertical permeabilities in the repository target area at -465 m elevation, according to the model of Svensson and Follin (2009, Figure 4-21). The white lines represent the main tunnels. Note that hydraulic conductor domains (HCDs) are included along with HRD fractures in these calculations, and account for the most conspicuous linear patterns of elevated permeability. The dark blue areas ($k < 2x10^{-16}$ m^2 corresponding approximately to $K < 2x10^{-9}$ m/s) can be compared to the dark green areas with $K < 10^{-9}$ m/s in the cross-sections at Z = -450 m in Figures 3.6-3.8 of this report. The lighter blue areas (approximately $2x10^{-9}$ m/s $< K < 2x10^{-8}$ m/s) represent higher-K portions of the rock mass outside of the target volume, and can be compared with the pale green areas with 10^{-9} m/s $< K < 10^{-8}$ m/s in Figures 3.6-3.8.

Hydraulic conductivities calculated by a permeameter method, as presented by Joyce et al. (2009), are reproduced in Figure 3.24. The values obtained for the HRDs in the target volume, at the repository level of about -470 m, are mainly in the range $1x10^{-11}$ m/s $< K < 3x10^{-11}$ m/s, according to the color scale. The upper end of this range represents about a 1.8 orders of magnitude decrease in the permeameter estimates of Joyce et al. (2009) relative to the geometric estimates of Svensson and Follin (2009).

This difference of about 1.8 orders of magnitude is larger than the typical difference found between geometric and permeameter estimates of K in this study (Figure 3.13), although differences of up to 1.5 orders of magnitude were found for the lower-K blocks that correspond to the target volume at repository depth. The permeameter estimates in the present study may be biased upward by flows through fractures that cut across the corners of the block, as discussed in Section 2.2.3.

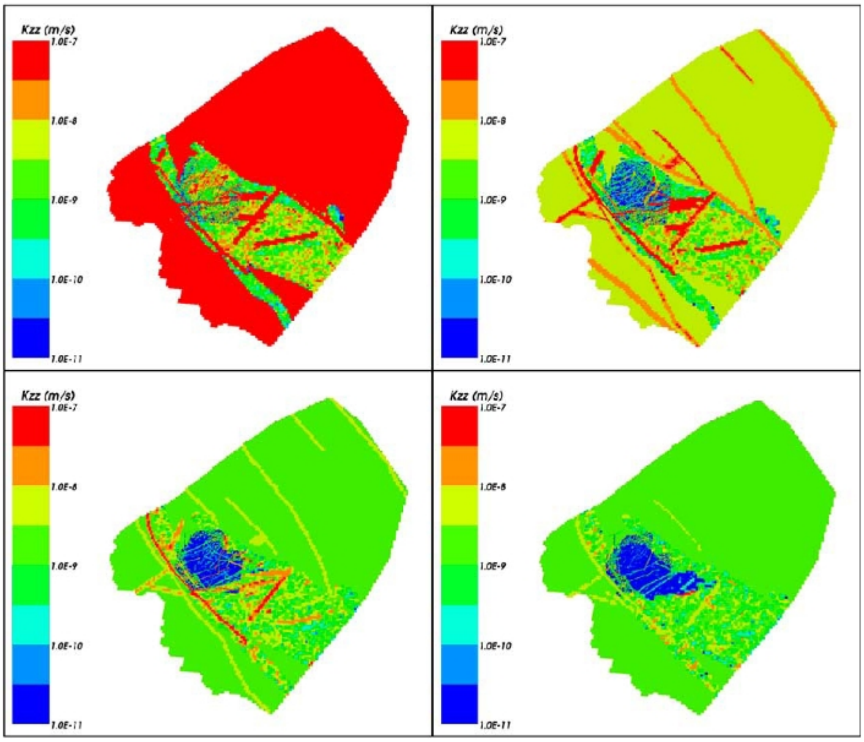

Figure 3.24 Calculated grid cell vertical hydraulic conductivity on horizontal slices through the regional-scale model of Joyce et al. (2009, Figure 4-3). Top left: at z = –80 m; Top right: at *z* = –250 m; Bottom left: *z* = –470 m; Bottom right: *z* = –700 m. Note that hydraulic conductor domains (HCDs) are included along with HRD fractures in these calculations, and account for the most conspicuous linear patterns of elevated permeability. The repository target area is just a small portion of these plots, approximately in the dark blue area of the lower left plot (*z* = -470 m). The dark blue areas (roughly 10^{-11} m/s < K < 3×10^{-11} m/s) can be compared to the geometric estimates of permeability of Svensson and Follin (2009) in Figure 3.23, and the corresponding cross-sections at Z = -450 m in Figures 3.6-3.8 of this report.

Additional differences may result from comparing vertical K values (as presented by SKB) with averages taken over the vertical and horizontal directions (as in Figure 3.13). The shift in anisotropy ratios for permeameter estimates (Figure 3.12) in comparison with geometric estimates (Figure 3.9) indicates that fracture connectivity effects are stronger in the vertical direction than for the horizontal directions.

Geometric estimates of kinematic porosity (meaning the porosity attributable to macroscopic, transmissive fractures that are included in the Hydro-DFN models, as considered in the geometric estimates of θ presented here) are presented by Svensson and Follin (2009, Figures 4-22, 4-23 and 4-25). Based on the c.d.f. of kinematic porosity in the last of these three figures, 95% of the grid blocks at repository depth have $\theta < 5 \times 10^{-5}$. Geometric estimates of θ based on an equivalent method in the present study are similarly dominated by values of $\theta < 5 \times 10^{-5}$, at the depth z = -450 m.

A corresponding plot of kinematic porosity at repository depth by Joyce et al. (2009, Figure 4-4), as reproduced here in Figure 3.25, shows θ predominantly in the range 1×10^{-5} to 3×10^{-5}. This is consistent with the geometric estimates of Svensson and Follin (2009), but several orders of magnitude higher than the flux-weighted estimates obtained from permeameter simulations in this study (Figure 3.14).

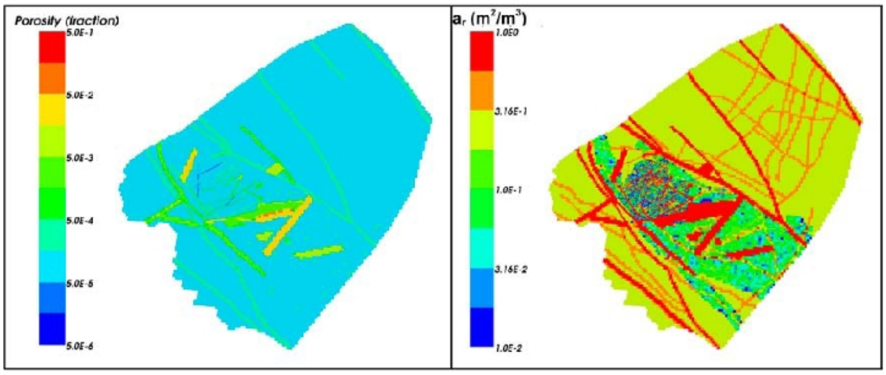

Figure 3.25 Calculated grid cell kinematic porosity and flow wetted surface area per unit volume of rock on a horizontal slice through the regional-scale model of Joyce et al. (2009, Figure 4-4) at *z* = –470 m. Note that hydraulic conductor domains (HCDs) are included along with HRD fractures in these calculations, and account for the most conspicuous linear patterns of elevated permeability. The depicted area is the same as in Figure 3.24.

Flow wetted surface estimates by Joyce et al. (2009) are also shown in Figure 3.25. Due to the scale of presentation and inclusion of HCDs, it is difficult to assess the variability of a_r estimates in the target volume. Most HRD blocks appear to have a_r in the range 0.06 to 0.3 m^{-1}, but this is very difficult to judge from the method of presentation that has been used. Values of 0.3 to 0.6 m^{-1} are specified for the rock mass outside of the volumes occupied by the HRDs, according to Table 2-6 of Selroos and Follin (2009). These are similar to the geometric estimates obtained for repository depths in the present study (Figure 3.3). The calculations given here also yield a few blocks with $a_r > 1$ m^{-1}.

According to the description of methodology by Joyce et al. (2009, p. 30), both porosity and flow-wetted surface were calculated as geometric estimates using formulae equivalent to those given in Section 2.2.2 of this report. Hence agreement with the geometric estimates of the same quantities by Svensson and Follin (2009) and in Section 3.1.2 of this report is expected.

SKB's hydrogeological modeling efforts do not seem to have applied any block-scale approach equivalent to the flux-weighted estimates, as developed in Section 2.2.3 and 3.1.3 of this report, which account for the likelihood that the majority of water (and hence solute) moving through the rock comes into contact only with a small portion of the fracture pore volume and surface area. The present results show that such an approach leads to much lower estimates of both porosity and flow-wetted surface, by several orders of magnitude. The lack of consideration of flux-weighted effects may lead to non-conservative predictions of solute-transport parameters (residence times and transport resistance *F*), so far as these are based on EPCM models that require block-scale values of θ and a_r. This is not an issue for calculations of the same transport parameters based on explicit DFN calculations that implicitly account for heterogeneous flow distribution within a given block.

Simulations of flow and transport through HRD blocks including tunnel EDZ and deposition holes, as presented in Section 3.2, yielded estimates of inflow rates to deposition holes and transport resistances *F* for solute particles tracks. Values of both inflow rates and *F* are partly a function of the simplified geometry and boundary conditions in the block-scale simulations (*i.e.* lacking HCDs and with assumed, nominal hydraulic gradients parallel to the block edges). In addition, SKB presents flows to deposition holes in terms of Darcy flux which are converted to “equivalent flowrates.” These factors complicate the possibility for detailed comparison with SKB's results.

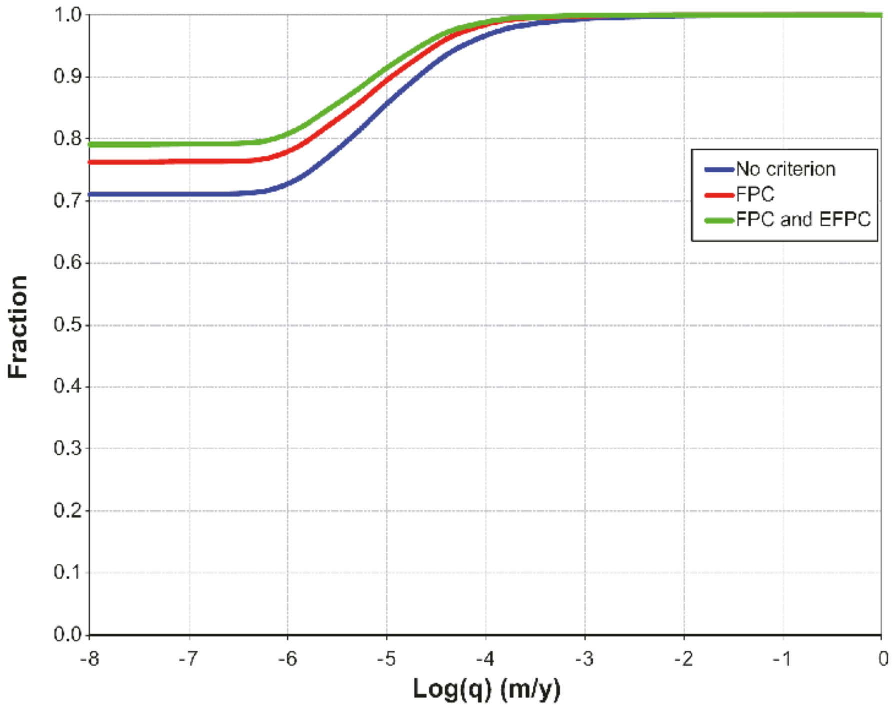

Figure 3.26 Cumulative distribution plot of Darcy flux (q) for the Q1 path at 2000 AD based on all deposition hole locations and applying different deposition hole rejection criteria, from Figure 5-10 of Selroos and Follin (2009). “FPC and EFPC” in the figure legend denotes that the “FPC or EFPC” criterion is applied.

Distributions of Darcy flux *q* to deposition holes for SKB's model of present-day, temperate conditions are shown in Figure 3.26 for different cases of deposition hole placement criteria. The FPC (full-perimeter intersection criterion) is most representative of the cases considered in the present report. For simplicity of comparison with the DFM model results presented in Section 3.2, the corresponding values of flowrate to deposition holes are taken as $Q \approx Aq$ where $A \approx 10\ m^2$ is taken as round, approximate value for the cross-sectional area of a deposition hole.

A comparison in these very approximate terms (Table 3.4) shows that the block-scale simulations in the present study yield a distribution of inflows that is broadly comparable to what could be expected from SKB's more complex and larger-scale model. The DFM block-scale model apparently has somewhat fewer “tight” deposition holes that carry no significant flow, but comparable percentages of deposition holes that exceed the higher flow values. Considering the approximate nature of this comparison as well as the large differences in model scales and boundary conditions, not too much importance should be attached to the differences. However, as a very rough, order-of-magnitude comparison, this gives some confidence that the DFM model and SKB's models are consistent in terms of flows to deposition holes.

Values of the transport resistance *F* for pathways through the DFN portion of SKB's model (Figure 3.26) have a median values of roughly $5x10^6$ to $6x10^6$ y/m, depending on the time of initial release, with a spread of about 4 orders of magnitude. The range of median values corresponds to a range of $1.6x10^{14}$ to $1.8x10^{14}$ s/m. This agrees well with *F* values for transport distances approaching 100 m in the block-scale models for the present study, as shown in Figures 3.20 through 3.22.

Table 3.4 Approximate comparison of distributions of flowrates to deposition holes as implied by Darcy fluxes for SKB's temperate-case model (as in Figure 3.26) with flowrates to deposition holes in block-scale simulations using the DFM model for the present study, for different directions of the hydraulic gradient, as presented in Figure 3.16, using the case with no EDZ. The conversion from Darcy flux to flowrate is based on a simple multiplication by a factor of 10 m^2 which is used as a round approximation for the cross-sectional area of a deposition hole.

Darcy flux q (m/y)	**Corresponding flowrate Q (L/y)**	**Percentage of deposition holes exceeding flux or flowrate value**			
		SKB (FPC case)	**DFM (gradient parallel to tunnel)**	**DFM (gradient perpendicular to tunnel)**	**DFM (vertical gradient)**
10^{-6}	0.01	70	60	60	65
10^{-5}	0.1	90	75	90	90
10^{-4}	1	97	90	95	97

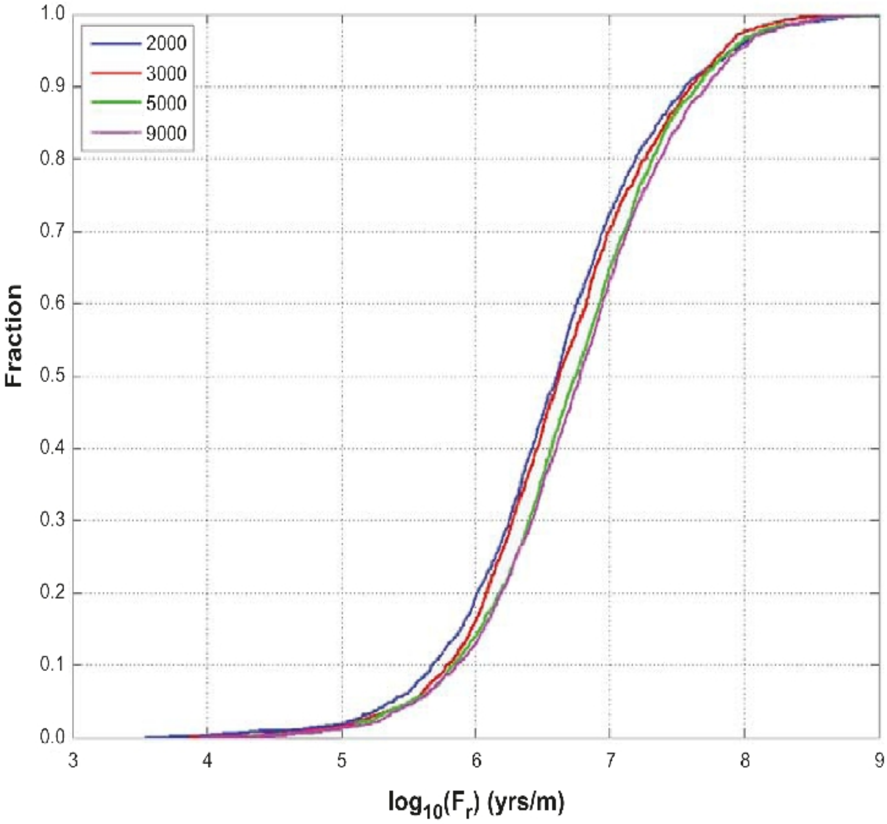

Figure 3.27 Cumulative distribution plot of DFN flow-related transport resistance (F) of the DFN portion of SKB's model for the Q1 path in the hydrogeological base case, for particles reaching the model top boundary (24%) released at 2000 AD, 3000 AD, 5000 AD and 9000 AD. From Figure 5-9 of Selroos and Follin (2009).

4. Conclusions

The principal results obtained from this modeling study consist of hydraulic and transport property estimates for discrete-fracture network (DFN) models on block scales of 50 m and 100 m, including blocks containing representative segments of deposition tunnels with deposition holes. These block scales are representative of the discretization used in equivalent continuum porous medium (ECPM) models of the Forsmark site in support of the license application.

Analytical, geometrical, and permeameter simulation methods are used to give multiple methods for estimating effective properties and understanding the significance of results.

Geometrical estimates of hydraulic conductivity, porosity and wetted surface for 50 m and 100 m block scales are comparable to analytical estimates based on models for fractures of infinite extent. However, the geometrical estimates of these properties, which take into account the finite extent of fractures as well as stochastic variation between blocks, are typically lower than the analytical estimates for the same depth intervals.

Comparison of geometrical estimates with permeameter simulations show that, for the DFN models and block scales the geometrical estimates of hydraulic conductivity (averaged over the three coordinate directions) tend to be higher than the permeameter estimates by about an order of magnitude for the lower part of the hydraulic conductivity range, but show better agreement for the more conductive blocks.

These results indicate a possibility to use geometrical estimation – possibly with an empirical adjustment for the lower-K blocks – as a relatively efficient method for simulating hydraulic conductivity fields for groundwater flow models based on continuum concepts.

However, limitations of the method are also identified in terms of the range and types of anisotropy that can be produced. Permeameter simulations indicate a likelihood of blocks for which the effective hydraulic conductivity is more strongly unidirectional than can be produced by the geometrical estimation method. Therefore, if the role of block-scale anisotropy for site-scale models is to be assessed as part of license application review, more computationally intensive approaches such as permeameter simulations will be required.

Flux-weighted estimates of porosity and wetted surface from permeameter simulations are found to be lower than the corresponding geometrical estimates of these parameters, by 3 to 4 orders of magnitude depending on the method of weighting. The flux-weighted estimates are likely to be more representative of the fraction of the fracture network that would be encountered by radionuclides released from the repository, even without taking physical channeling into account. Lower values of these parameters can lead to reduced estimates of geosphere retention. Hence it appears to be important to review how effective values of these properties are derived for use in ECPM models of the Forsmark site.

Simulations of flow for a deposition tunnel embedded in block-scale simulations of the DFN at repository depth indicate that even an EDZ that is partly discontinuous can have a significant effect on directional hydraulic conductivity parallel to the tunnel axis, apparently by increasing connectivity of the fracture network. However, the influence of the EDZ for flow in other directions is negligible.

Block-scale transport simulations by particle tracking indicate that an EDZ in the floor of a deposition tunnel, when present, is the dominant path for advective-dispersive transport. The block-scale simulations support previous site-scale modeling results which indicated that particles released from one deposition hole tend to migrate to the next deposition hole, for the sparsely fractured rock mass that is interpreted to exist at repository depths at Forsmark. Reduction of continuity of the EDZ can lead to more complex solute trajectories in this direction. However for cases in which the areal persistence of the EDZ is 50% or greater, the results in terms of transport resistance on the block scale are not strongly affected.

The geometrical and permeameter estimates of hydraulic conductivity obtained in this study are broadly consistent with the respective comparable results from SKB's hydrogeological models for SR-Site. SKB has not presented comparable information about block-scale anisotropy. The results obtained here indicate that the geometrical estimation method (as used in SKB's hydro-DFN calibration process) tends to underestimate the ratio of horizontal to vertical hydraulic conductivity. This might partly explain why an adjustment of this ratio was necessary to improve the performance of SKB's hydro-DFN model.

The geometrical estimates of porosity and flow wetted surface, as obtained in this study, are also broadly consistent with SKB's corresponding estimates. SKB has not produced estimates that account for likelihood that the majority of water (and hence solute) moving through the rock comes into contact with only a small portion of the fracture network. This may lead to non-conservative estimates of solute transport parameters (residence times and transport resistance *F*), to the extent that these are based on ECPM models that utilize block-scale values of porosity and flow wetted surface. However this is not a concern for SKB's calculations that are based entirely on explicit DFN calculations, which implicitly account for heterogeneous flow distributions in the fracture networks.

Block-scale simulations to simulated tunnels and deposition holes in the present study yield distributions of inflows that are reasonably similar to those predicted by SKB's more complex, larger-scale models. Transport resistances (*F*) for scales approaching 100 m, in the block-scale simulations, are also broadly similar to *F* values for the DFN portion of SKB's models.

Thus the results of this study are generally consistent with the comparable predictions of SKB's hydro-DFN models. It should be noted that this consistency is based on calculations that are based on SKB's underlying DFN conceptual model for the target volume at Forsmark. Alternative DFN conceptual models such as considered in a previous study (Geier, 2011) could yield larger differences.

5. References

Ahlstrom, S. W., Foote, H. P., Arnett, R. C., Cole, C. R., and Serne, R.J., 1977. Multicomponent mass transport model. Theory and numerical implementation (discrete parcel random walk version), Battelle report BNWL for ERDA, Columbus, Ohio.

Berkowitz, B., Nauman, C., and Smith, L., 1994. Mass transfer at fracture intersections: An evaluation of mixing models. *Water Resources Research*, v. 30, p. 1765-1773.

Brantberger, M., Zetterqvist, A., Anbjerg-Nielsen, Olsson, T., Outters, N., and Syrjänen, P., 2006. Final repository for spent nuclear fuel: Underground design Forsmark, Layout D1. SKB Report R-06-34, Swedish Nuclear Fuel and Waste Management Co., Stockholm.

Dverstorp, B., Geier, J., and Voss, C., 1996. Simple evaluation of groundwater flux and radionuclide transport at Äspö (SITE-94): SKI Report 96:14, Swedish Nuclear Power Inspectorate, Stockholm.

Follin, S., 2008. Bedrock hydrogeology Forsmark. Site descriptive modelling, SDM-Site Forsmark. SKB R-08-95, Swedish Nuclear Fuel and Waste Management Co., Stockholm.

Geier, J., 2008. Discrete Feature Model (DFM) user documentation. SKI Report 2008:57, Swedish Nuclear Power Inspectorate, Stockholm.

Geier, J., 2010. Discrete-feature model implementation of SDM-Site Forsmark. SSM Report 2010:05, Swedish Radiation Safety Authority, Stockholm.

Geier, J., 2011. Investigation of discrete-fracture network conceptual model uncertainty at Forsmark. SSM Report 2011:13, Swedish Radiation Safety Authority, Stockholm.

Geier, J., 2012. Hydrogeological characteristics of sites for low- and intermediate-level waste disposal. SSM Report 2012:49, Swedish Radiation Safety Authority, Stockholm.

Joyce, S., Simpson, T., Hartley, L., Applegate, D., Hoek, J., Jackson, P., Swan, D., Marsic, N., and Follin, S., 2009. Groundwater flow modelling of periods with temperate climate conditions – Forsmark. SKB Report 2009-20, Swedish Nuclear Fuel and Waste Management Co., Stockholm.

Long, J.C.S., Remer, J.S., Wilson, C.R., and Witherspoon, P.A., 1982. Porous media equivalents for networks of discontinuous fractures, *Water Resources Research*, Vol. 18, No. 3, P. 645. doi:10.1029/WR018i003p00645.

Munier R, 2010. Full perimeter intersection criteria. Definitions and implementations in SR-Site. SKB TR-10-21, Swedish Nuclear Fuel and Waste Management Co., Stockholm.

Oda, M., 1985. Permeability tensor for discontinuous rock masses. *Geotechnique*, Vol. 35., No. 4, p. 483-495.

Selroos, J-O., and Follin, S., 2009. SR-Site groundwater flow modelling methodology, setup and results. SKB R-09-22, Swedish Nuclear Fuel and Waste Management Co., Stockholm.

SKB, 2008. SDM-Site site description of Forsmark at completion of the site investigation phase, SDM-Site Forsmark. SKB R-08-05, Swedish Nuclear Fuel and Waste Management Co., Stockholm.

Stephens, M.B., Fox, A., La Pointe, P., Simeonov, A., Isaksson, H., Hermanson, J., and Öhman, J., 2007. Geology Forsmark. Site descriptive modelling Forsmark stage 2.2. SKB R-07-45, Swedish Nuclear Fuel and Waste Management Co., Stockholm.

Svensson, U., and Follin, S., 2009. Groundwater flow modelling of the excavation and operational phases – Forsmark. SKB R-09-19, Swedish Nuclear Fuel and Waste Management Co., Stockholm.

Tsang, Y.W., Tsang, C. F., Hale, F.V., and Dverstorp, B., 1996. Tracer transport in a stochastic continuum model of fractured media. *Water Resources Research*, Vol. 32, No. 10, p. 3077, doi:10.1029/96WR01397.

Vidstrand, P., Follin, S., and Zugec, N., 2010. Groundwater flow modelling of periods with periglacial and glacial climate conditions – SR-Site Forsmark. SKB R-09-21, Swedish Nuclear Fuel and Waste Management Co., Stockholm.

2012:67

The Swedish Radiation Safety Authority has a comprehensive responsibility to ensure that society is safe from the effects of radiation. The Authority works to achieve radiation safety in a number of areas: nuclear power, medical care as well as commercial products and services. The Authority also works to achieve protection from natural radiation and to increase the level of radiation safety internationally.

The Swedish Radiation Safety Authority works proactively and preventively to protect people and the environment from the harmful effects of radiation, now and in the future. The Authority issues regulations and supervises compliance, while also supporting research, providing training and information, and issuing advice. Often, activities involving radiation require licences issued by the Authority. The Swedish Radiation Safety Authority maintains emergency preparedness around the clock with the aim of limiting the aftermath of radiation accidents and the unintentional spreading of radioactive substances. The Authority participates in international co-operation in order to promote radiation safety and finances projects aiming to raise the level of radiation safety in certain Eastern European countries.

The Authority reports to the Ministry of the Environment and has around 270 employees with competencies in the fields of engineering, natural and behavioural sciences, law, economics and communications. We have received quality, environmental and working environment certification.

Strålsäkerhetsmyndigheten
Swedish Radiation Safety Authority

SE-171 16 Stockholm
Solna strandväg 96

Tel: +46 8 799 40 00
Fax: +46 8 799 40 10

E-mail: registrator@ssm.se
Web: stralsakerhetsmyndigheten.se